Global and Planetary Change 255 (2025) 105085

Contents lists available at ScienceDirect

Global and Planetary Change

journal homepage: www.elsevier.com/locate/gloplacha

Research Article

A multi-basin comparison of paleoredox conditions during the mid-Silurian Mulde/*lundgreni* event☆

Mahdi Maaleki-Moghadam [a,*], Anders Lindskog [a,b], Paula J. Noble [c], Dimitri Kaljo [d], Olle Hints [d], John T. Goodin [a], Jeremy D. Owens [a], Seth A. Young [a]

[a] Department of Earth, Ocean, and Atmospheric Science and National High Magnetic Field Laboratory, Florida State University, Tallahassee, Florida, USA
[b] Department of Environmental Science, Kristianstad University, Kristianstad, Sweden
[c] Geological Sciences & Engineering, University of Nevada, Reno, Nevada, USA
[d] Department of Geology, Tallinn University of Technology, Ehitajate Tee 5, 19086 Tallinn, Estonia

ARTICLE INFO

Editor: Dr. Maoyan Zhu

Keywords:
Silurian
Mulde/lundgreni event
Paleoredox
Iron speciation
Trace metals
Pyrite sulfur isotopes
Ocean anoxia

ABSTRACT

The mid-Silurian Mulde/*lundgreni* Event was characterized by a widespread biotic crisis among marine taxa (e.g., graptolites, conodonts), associated with a notable double-peaked positive carbon isotope excursion. These biotic and chemical signatures provide evidence that this time interval experienced significant environmental change. While there has been significant research on this critical interval within the Silurian, the oceanic redox conditions encompassing this event remain poorly constrained. Here, we utilize a multiproxy approach to investigate the paleoredox dynamics within two geographically distinct marine basins and paleocontinents spanning the Mulde/*lundgreni* Event: Abbott River, Twilight Creek (Arctic Canada, Laurentia), and the Priekule-20 core (Latvia, Baltica). We present new organic carbon isotopes ($\delta^{13}C_{org}$), pyrite sulfur isotopes ($\delta^{34}S_{pyr}$), iron speciation, and trace metal data to reconstruct regional marine paleoredox conditions from three separate localities providing a more global view. Our geochemical records reveal synchronous positive excursions in $\delta^{13}C_{org}$ and $\delta^{34}S_{pyr}$ across all sections, indicating increased burial of organic carbon and pyrite. Iron speciation data suggest persistently ferruginous anoxic bottom waters in Laurentia throughout the study interval. In contrast, bottom water redox conditions in Baltica were more variable, fluctuating from possibly oxic to ferruginous anoxic conditions during the Mulde carbon isotope excursion (CIE). Trace metal patterns include an initial enrichment followed by a reduction in all sections suggesting a drawdown during the first Mulde CIE peak, a renewed enrichment during biotic recovery, and a second decrease indicating another drawdown coinciding with the second Mulde CIE peak. Importantly, this two-step enrichment–drawdown pattern mirrors the double-peaked nature of the Mulde CIE, and thereby suggests globally dynamic bottom water conditions. Mo and U enrichment factors suggest differing degrees of restriction, but shared temporal trends still imply a global redox signal. These results support a model in which climate-driven sea-level fluctuations modulated marine deoxygenation, contributing to the timing and selectivity of extinctions among hemipelagic and planktonic taxa.

1. Introduction

Despite being the shortest period of the Paleozoic Era, the Silurian stands out as a time of intense evolutionary and environmental change, punctuated by a series of dramatic sea-level fluctuations and biotic crises that significantly impacted marine ecosystems (Kaljo and Märss, 1991; Cramer et al., 2011; Melchin et al., 2020). Recurrent intervals of environmental upheaval commonly coincide with perturbations of the global carbon cycle (Jeppsson, 1998; Saltzman, 2001; Cramer et al., 2012; McAdams et al., 2019). The connections between intervals of biotic turnover to marine redox conditions, atmospheric O_2 and CO_2 levels, and continental weathering rates are poorly constrained for much of the Silurian (Krause et al., 2018; Bowman et al., 2019; Sproson et al., 2022). Only a very few intervals within the Silurian have been investigated in enough detail to provide some information about the marine redox state at the global and/or local scale (Bowman et al., 2019; Young et al., 2019;

☆ This article is part of a Special issue entitled: 'Oceanic Anoxic Event' published in Global and Planetary Change.

* Corresponding author.
E-mail address: mm21e@fsu.edu (M. Maaleki-Moghadam).

https://doi.org/10.1016/j.gloplacha.2025.105085
Received 1 May 2025; Received in revised form 11 September 2025; Accepted 15 September 2025
Available online 16 September 2025

Stockey et al., 2020; Wang et al., 2024).

Among the Silurian biotic crises, the earliest identified was a significant extinction event affecting graptolites (a major early Paleozoic zooplankton group), initially named the "Big Crisis" (Jaeger, 1959). During the early to middle Homerian Age of the Wenlock Epoch, mid-Silurian, this extinction reached its maximum intensity, and is more commonly referred to as the *lundgreni* Event; the latter name is derived from the graptolite biozone *Cyrtograptus lundgreni*, in which the extinction reaches its peak at the end of this Zone (Koren, 1991; Porębska et al., 2004). The interval is also known as the Mulde Event, named after an area on the island of Gotland, Sweden (e.g., Jeppsson and Calner, 2002). Coincident with this biotic crisis, a distinctive geochemical signature was identified: a double-peaked positive carbon isotope excursion (CIE) (Kaljo et al., 1997; Saltzman, 2001; Calner et al., 2006; Cramer et al., 2006; Noble et al., 2012; Danielsen et al., 2019) recorded in both carbonate ($\delta^{13}C_{carb}$) and organic carbon ($\delta^{13}C_{org}$) isotope records. These global $\delta^{13}C$ records suggest significant perturbations to the global carbon cycle coincident, at least in part, with the marine extinction event (Biebesheimer et al., 2021). Despite the global recognition of the Mulde CIE (also known as the Homerian CIE; e.g., Manda et al., 2019; Ray et al., 2019), there is no consensus about the underlying causal mechanism(s). Other studies have proposed eustatic sea-level changes, ocean circulation shifts, and volcanic activity as potential mechanisms, but a definitive explanation remains elusive (Munnecke et al., 2010; Cramer et al., 2012). Conodont-phosphate oxygen isotope data indicate a global cooling event during this interval of the mid-Silurian, and it has been proposed as a potential causal mechanism (Trotter et al., 2016). However, there is a lack of corroborating evidence in the geological record, such as glacial sediments, to support this hypothesis. Furthermore, it remains unclear how temperature change alone would mechanistically drive the associated perturbation of the global carbon cycle.

Most geochemical investigations of the Mulde CIE and the associated extinction event have focused primarily on carbon isotope records (Noble et al., 2005, 2012; Cramer et al., 2006; Biebesheimer et al., 2021), and there is a notable absence of comprehensive marine paleoredox studies for this critical interval. This gap in our understanding limits our ability to fully comprehend the environmental changes associated with the Mulde/*lundgreni* Event and their potential role in driving the documented biotic crisis. The present study aims to address this knowledge gap by employing a multiproxy approach to investigate potential redox changes during the Mulde CIE and associated extinction events. We utilize iron speciation, redox sensitive trace metal geochemistry, and pyrite sulfur isotopes ($\delta^{34}S_{pyr}$) to evaluate whether significant changes in regional oceanic oxygen levels played a role in the mid-Silurian Mulde/*lundgreni* Event. Specifically, this multiproxy approach may allow us to distinguish different intervals within the marine redox ladder in these specific regions (e.g., Bowman et al., 2021). This study focuses on three geographically distinct sections, where the extinction event and CIE have been previously well-documented, to provide a more comprehensive understanding of different paleoenvironmental settings and ocean basins throughout the Mulde/*lundgreni* Event. Two outcrop sections from the northern margin of Laurentia are examined: the Abbott River and the Twilight Creek sections located in present-day Arctic Canada. Additionally, we analyzed samples from the Priekule-20 core in Latvia, representing the paleocontinent of Baltica. This comprehensive marine paleoredox investigation will provide new insights into the local to regional environmental conditions surrounding this major Silurian biotic crisis and contribute to our understanding of the complex interplay between geochemical perturbations and biological extinctions in Earth's history.

2. Background

2.1. Geological setting

The three study sections outcrop along Abbott River on Cornwallis Island and Twilight Creek on Bathurst Island regions of modern-day Arctic Canada, and the Priekule-20 core succession within the subsurface of western Latvia (Fig. 1). The Cape Phillips Formation, which includes the Abbott River and Twilight Creek sections, accumulated in a deep marine basinal environment. This depositional setting was located offshore from the Franklinian Shelf, along the northern margin of the paleocontinent of Laurentia (Noble et al., 2012; Melchin et al., 2013). This margin of the Laurentian Craton was characterized by the accumulation of carbonate and clastic sediments from the late Cambrian to the Devonian, primarily in a passive margin environment (Trettin, 1989; Harrison et al., 1999). The Abbott River section on Cornwallis Island's western coast exemplifies a more proximal depositional environment close to the basin's edge, roughly 25 km from the shelf–slope transition (Noble et al., 2012). The Twilight Creek section on Bathurst Island is located more than 100 km northwest of the shelf–slope transition, representing a more distal, deeper basin environment (Noble et al., 2012). The Abbott River section is characterized by thin to medium-bedded platy mudstone and shale that is calcareous to dolomitic, interlayered with thicker layers of bioclastic wackestone. Calcareous and dolomitic concretions are widespread throughout the section, containing well-preserved graptolites (Lenz et al., 2006; Noble et al., 2012). The Twilight Creek section, by comparison, consists of organic-rich, thinly bedded platy calcareous mudstone and graptolitic shale. The Cape Phillips Formation in this region spans the Hirnantian (latest Ordovician) through Pridoli (latest Silurian), with the Wenlock represented by over 100 m of continuous exposure at Twilight Creek (Lenz et al., 2006; Noble et al., 2012).

The Priekule-20 core site is located in modern-day Latvia represents a deep shelf setting within the Baltoscandian paleobasin, which during the Silurian was part of a tropical, epicratonic seaway on the southern edge of the paleocontinent Baltica (Kiipli et al., 2010). The Priekule-20 succession spans the Rhuddanian to Ludfordian stages of the Silurian, encompassing a thickness of 436 m. The studied interval includes the Riga Formation, corresponding to the *Cyrtograptus lundgreni* graptolite biozone, followed by the Siesartis Formation, which includes the *Gothograptus nassa-Colonograptus ludensis* graptolite biozones. Above this lies the Dubysa Formation, containing the Nova Beds in its upper part. The succession primarily consists of gray shales and marlstones, with occasional argillaceous limestone interbeds, indicative of a deep shelf environment characterized by low oxygen levels at the seabed, as evidenced by the absence of bioturbation in the shales (Kaljo et al., 1997; Kiipli et al., 2010).

2.2. Framework for redox interpretations

2.2.1. Pyrite sulfur isotopes

The sulfur cycle is a fundamental regulator of Earth's redox conditions through geological time. In modern oceans, sulfate (SO_4^{2-}) constitutes one of the most abundant dissolved ionic species and operates as a critical terminal electron acceptor in microbial sulfate reduction (MSR). During MSR, microorganisms exhibit preferential utilization of lighter sulfur isotopes in their metabolic processes, analogous to biological carbon isotope fractionation. While organic matter typically functions as the primary substrate for MSR, these microorganisms can also metabolize methane in environments where organic matter is scarce (Canfield, 2001; Amend et al., 2004). The principal product of MSR, hydrogen sulfide (H_2S), readily combines with available iron to form

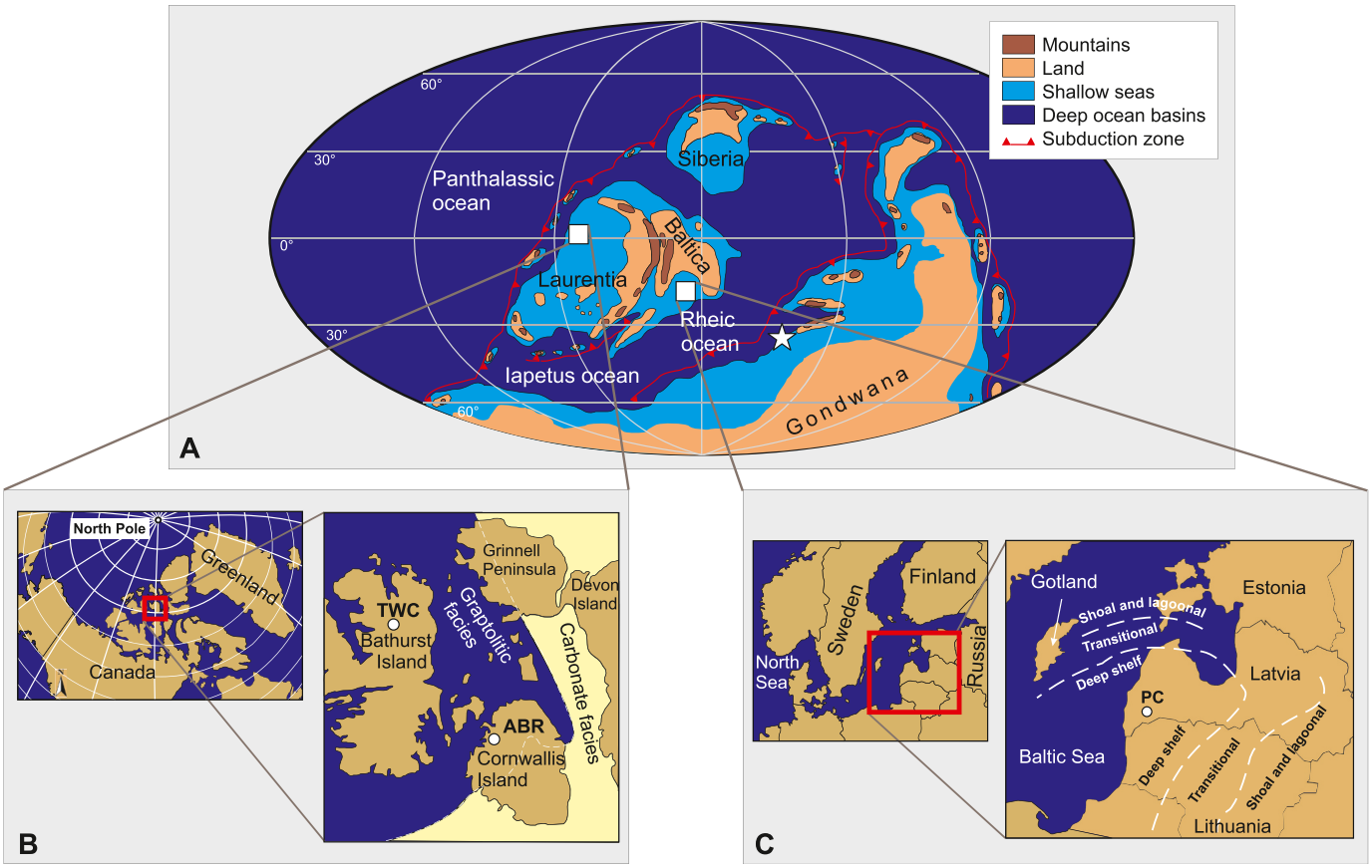

Fig. 1. Locality maps for all successions investigated in this study. A) Paleogeographic reconstruction of the middle Silurian showing the approximate locations of the studied sections from Arctic Canada (Abbott River and Twilight Creek) and Latvia (Priekule-20 core). The star indicates the approximate location of the Prague Basin (Perunica terrane; Frýda and Frýdová, 2025), which is discussed in the text for comparison (Modified after Scotese, 2014). B) Present-day locations of studied sections at Abbott River (ABR) and Twilight Creek (TWC) in Arctic Canada (Modified after Noble et al., 2012). C) Present-day location of Priekule-20 core (PC) in western Latvia (Modified after Kiipli et al., 2010).

pyrite in both water columns and sediments. Pyrite burial represents a key control on atmospheric oxygen levels over geological timescales – its longterm burial releases O_2 to the atmosphere, while its oxidation consumes O_2 (Lyons and Gill, 2010). This process is intrinsically linked to carbon cycling, as the organic matter utilized in MSR originates from photosynthetic organisms. Unlike oxic remineralization, which returns fixed carbon to CO_2, MSR ultimately leads to pyrite formation through H_2S production and subsequent reaction with Fe^{2+}. The isotopic composition of sedimentary pyrite ($\delta^{34}S_{pyr}$) provides crucial insights into ancient marine redox conditions and sulfur cycling. Enhanced pyrite burial through increased MSR activity typically results in more positive $\delta^{34}S_{pyr}$ values, while more limited MSR and pyrite formation often correspond to lighter isotopic signatures. Variations in pyrite sulfur isotopes document changes in marine redox conditions and microbial sulfur cycling throughout Earth's history (Gill et al., 2007).

2.2.2. *Iron geochemistry*

Iron is an essential element for fundamental biological processes and plays a crucial role in Earth's biogeochemical cycles. It serves as a key component in electron transfer during photosynthesis, acts as a cofactor in nitrogen fixation, and is vital for respiratory proteins and various enzymatic processes (Raiswell and Canfield, 2012). The cycling of iron in marine systems is intimately linked to the sulfur cycle, and its different oxidation states make it particularly sensitive to changes in environmental redox conditions (Poulton and Canfield, 2011). Iron speciation has emerged as one of the most widely applied paleoredox proxies, uniquely capable of distinguishing between three major oceanic redox states - ferruginous (anoxic, containing dissolved ferrous Fe), and euxinic (anoxic, containing dissolved sulfide) (Poulton and Canfield, 2011), and by oxygenated conditions (albeit not direct evidence but rather due to elimination of the other two redox conditions). The proxy is built upon decades of research into the biogeochemical behavior of iron and sulfur during early diagenesis and is based on operationally defined iron pools that exhibit different reactivities towards dissolved sulfide (Canfield et al., 1992; Poulton and Canfield, 2005). The highly reactive iron pool (Fe_{HR}) consists of iron phases that readily react with sulfide on early diagenetic timescales, including iron carbonate, iron (oxyhydr)oxides, magnetite, and iron sulfides (Poulton et al., 2004; Poulton and Canfield, 2005). The utility of iron speciation stems from characteristic enrichments of Fe_{HR} in sediments deposited under anoxic conditions relative to oxic settings. Modern and ancient sediments deposited under oxic conditions typically show Fe_{HR}/Fe_T ratios below

0.38, while anoxic settings commonly have ratios exceeding this threshold (Raiswell and Canfield, 1998; Poulton and Raiswell, 2002). Within anoxic settings, further refinement of bottom water redox conditions can be made based on the ratio of pyrite iron to highly reactive iron (Fe_{pyr}/Fe_{HR}). Ratios >0.6–0.8 commonly indicate euxinic conditions (Anderson and Raiswell, 2004; März et al., 2008; Benkovitz et al., 2020), whereas ratios ≤0.6 suggest ferruginous conditions (Poulton and Canfield, 2011; Poulton, 2021). In euxinic environments like the modern Black Sea, these enrichments occur through the water-column formation of iron sulfides, with additional dissolved or reactive particulate Fe supplied via release from sediments on the shallower shelf through a mechanism termed the "shelf-to-basin Fe shuttle" (Anderson and Raiswell, 2004; Lyons and Severmann, 2006).

2.2.3. Trace metal geochemistry

Molybdenum (Mo) has emerged as a particularly useful proxy due to its consistent modern seawater concentration (~107 nM), well-understood behavior under different redox conditions (e.g., Tribovillard et al., 2006), and relatively long modern residence time of ~450 kyr (e.g., Miller et al., 2011). Mo requires strongly reducing, sulfidic conditions for significant enrichment with euxinic (anoxic and sulfidic waters) being more enriched. In oxic waters, Mo exists as stable molybdate (MoO_4^{2-}) ions. However, in the presence of euxinic waters, Mo is efficiently sequestered in sediments through the reduction of molybdate to thiomolybdates (MoO^xS_{4-x}, where x = 0 to 3), which are particle-reactive and prone to scavenging by sulfides and sulfur-rich organic molecules (Tribovillard et al., 2006).

Vanadium (V) is a redox sensitive trace metal that can become enriched in mildly reducing environments with anoxic water columns lacking free hydrogen sulfide and, in the modern ocean, is characterized by a smaller reservoir size and shorter residence time (~50–100 kyr) compared to Mo (Algeo, 2004). This occurs as V(V) undergoes reduction to V(IV), producing compounds like vanadyl ions (VO_2^+) or hydroxyl species (e.g., $VO(OH)^{3-}$). These forms of vanadium can accumulate in sediments via surface adsorption or by creating organometallic complexes. When conditions become more strongly reducing (e.g., anoxic + free hydrogen sulfide = euxinic), V experiences further reduction to V (III), potentially precipitating as oxide (V_2O_3) or hydroxide ($V(OH)_3$) phases (Algeo and Maynard, 2004; Owens et al., 2017). The initial reduction of V occurs under low oxygen conditions and is not dependent upon the presence of sulfide, and thus has been used to potentially indicate changes in local/global anoxia when paired with other proxies that can track sulfidic conditions (Owens et al., 2016; Kozik et al., 2023).

Manganese (Mn) shows opposite behavior under reducing conditions compared to Mo and V. Under oxic conditions, dissolved Mn(II) is oxidized to form insoluble Mn(III,IV) oxyhydroxides that serve as important carriers for other trace metals through scavenging processes (Calvert and Pedersen, 1996). Under reducing conditions, Mn-oxyhydroxides become unstable and dissolve, releasing both Mn and the scavenged trace metals back into solution. Because Mn-oxide minerals require oxygen for formation, they cannot be preserved under anoxic or euxinic conditions, leading to Mn depletion in sediments deposited under reducing conditions (Tribovillard et al., 2006). The transformation between oxidized and reduced forms is particularly sensitive to oxygen availability – Mn(III/IV) rapidly converts to Mn^{2+} when oxygen concentrations decline (Rue et al., 1997; Algeo and Maynard, 2008). Therefore, sedimentary Mn concentrations above average crustal values of 850 ppm typically indicate more oxidizing depositional environments (Turgeon and Brumsack, 2006; Boyer et al., 2011).

3. Materials and methods

A total of 84 samples were collected: 27 from the Abbott River section, 24 from the Twilight Creek section, and 33 from the Priekule-20 core. Stratigraphic intervals with notable diagenetic alteration (i.e., recrystallization, pyritization, or iron oxide staining) were avoided while sampling. All samples were cleaned three times with ultra-pure water (deionized, distilled; 18.2 MΩ) in an ultrasonic bath to remove weathered portions and surficial contaminants. Subsequently, approximately 5–10 g of each sample were powdered using an agate mortar and pestle and splits of each sample were used for the following analyses.

3.1. Carbon isotopes

For the Priekule-20 core, each sample (approximately 0.5 g of powder) was treated with 6 N HCl to eliminate carbonate minerals. The samples underwent three cycles of acidification and rinsing with ultra-pure water (18.2 MΩ), followed by overnight drying at 70 °C. The dried residues were homogenized and encapsulated in tin for isotopic analysis. The $\delta^{13}C_{org}$ measurements were performed using an elemental analyzer (Carlo Erba) interfaced with an isotope ratio mass spectrometer (ThermoFinnigan Delta Plus XP) via a Conflo III system at the National High Magnetic Field Laboratory, Florida State University (NHMFL-FSU). Data calibration and sample precision were monitored through regular analysis of laboratory standards, which are calibrated against International Atomic Energy Agency (IAEA) standards. Results are expressed in standard delta-notation (δ) as per mill (‰) relative to Vienna Pee Dee Belemnite (VPDB). The organic carbon isotope standards used at NHMFL-FSU included Acetanilide ($\delta^{13}C = -29.2$ ‰), Urea-2 ($\delta^{13}C = -8.3$ ‰), and WYSTD ($\delta^{13}C = -12.7$ ‰). The analytical precision for $\delta^{13}C_{org}$ and %C was ±0.2 ‰ and ± 0.7 % (1σ) or better, respectively. Total organic carbon (TOC) content was determined by comparing CO^{2+} ion beam intensities (masses 44, 45, and 46) between unknown samples and the gravimetric standard acetanilide analyzed in the same sequence. The uncertainty for TOC measurements was less than ±5 %.

3.2. Pyrite extraction and sulfur isotope analyses

Pyrite sulfur was extracted from all samples using a modified version of the chromium reducible sulfur extraction method described by (Brüchert and Pratt, 1996). For each sample, 0.5–2.0 g of powdered sample was placed in a glass extraction vessel and reacted with a solution containing 70 mL of 12 M HCl and 30 mL of 1.0 M $CrCl_2$. This mixture was heated and stirred continuously for 2–3 h. The resultant H_2S gas was first carried via $N_{2(g)}$ through a 0.1 M sodium citrate solution (pH 4), then through a 0.1 M $AgNO_3$ solution to form Ag_2S precipitate. This precipitate was collected by filtration, washed with ultrapure water (18.2 MΩ), dried, and weighed to determine concentration. The mass of Ag_2S precipitate was used to calculate the weight percentage of pyrite in the sample, assuming complete conversion of FeS_2 to Ag_2S. These data were then used to derive the pyrite iron content (Fe_{pyr}). Isotopic analysis of pyrite sulfur was performed using an elemental analyzer (Thermo-Isolink) coupled to an isotope ratio mass spectrometer (Thermo Delta V Plus) via a Dual Inlet system. Calibration and precision were assessed using laboratory standards referenced to IAEA standards. Results are reported in delta notation (δ) as per mill (‰) relative to Vienna Canyon Diablo Troilite (VCDT). The sulfur isotope standards used at NHMFL-FSU included IAEA S-3 ($\delta^{34}S = -32.3$ ‰), PQM2 (−16.0 ‰), ERE Ag_2S (−4.7 ‰), EMR-CP (0.9 ‰), SWP (20.7 ‰), and PQB-D (40.5 ‰). The analytical precision for $\delta^{34}S_{pyr}$ measurements was ±0.2 ‰ or better.

3.3. Iron speciation

Iron speciation analysis was conducted on all samples used for pyrite isotope measurements, following the methodology described by (Poulton and Canfield, 2005). For each sample, approximately 0.1 g of powder was placed in a clean 15 mL centrifuge tube. The sequential extraction process involved three main steps. First, carbonate-associated iron (Fe_{carb}) was extracted using 10 mL of 1.0 M sodium acetate (pH 4.5) for 48 h of continuous shaking. Following this, iron from oxides and oxyhydroxides (Fe_{ox}) was extracted using 10 mL of 0.29 M sodium dithionite (pH 4.8, buffered with 0.35 M acetic acid and sodium citrate) for 2 h of constant shaking. Finally, magnetite-associated iron (Fe_{mag}) was extracted using a mixture of 0.2 M ammonium oxalate and 0.17 M oxalic acid (pH 3.2, adjusted with ammonium hydroxide) for 6 h of continuous shaking. After each extraction step, samples were centrifuged, and the supernatant was collected for analysis.

Samples were rinsed with ultrapure water (18.2 MΩ resistivity), centrifuged, and decanted between extractions. The extracted solutions were diluted with 2 % ultrapure HNO3 and analyzed for iron concentrations using an Agilent 7500cs inductively-coupled plasma mass spectrometer (ICP-MS) at the National High Magnetic Field Laboratory, Florida State University (NHMFL-FSU) and Agilent 7900 Quadrupole ICP-MS at the University of California–Riverside. The total highly reactive iron (Fe_{HR}) was calculated as the sum of all extracted iron species: $Fe_{HR} = Fe_{carb} + Fe_{ox} + Fe_{mag} + Fe_{pyr}$, where Fe_{pyr} represents pyrite-associated iron determined in previous analyses.

3.4. Trace metals

Trace metal concentrations were determined for the same sample set previously analyzed for iron speciation and pyrite isotopes. The analytical process began with approximately 100 mg of each sample being weighed into ceramic crucibles and heated to 500 °C for ~15 h to eliminate volatile and reactive organic matter in the samples. The resulting residues were then transferred to Savillex beakers for multi-acid digestion. Following this, the samples underwent a series of treatments with ultra-pure acids and oxidizing agents, including HNO_3, HCl, HF, and hydrogen peroxide. Each treatment involved a reaction period of 24–48 h at elevated temperatures (120–180 °C), with complete drying between each acid addition. After achieving total dissolution, the samples were dried once more and reconstituted in a 2 % HNO_3 solution. Trace metal analyses were performed using an Agilent 7500cs ICP-MS and a Thermo Element 2 instrument at the NHMFL-FSU. To ensure analytical accuracy, USGS standards SDO-1, SCO-1, and SGR-1 were processed and analyzed alongside the samples. The trace metal concentrations are reported in parts per million (ppm), with an analytical precision of ±5 % or better for Mo, V, Fe, and Mn.

We have also calculated enrichment factors, from our determined trace metal concentrations (described above), to assess authigenic enrichments of given redox sensitive trace metals with varying upper continental crust concentrations, by normalizing a given trace metal to aluminum. This method, adapted from (Algeo and Tribovillard, 2009) approach, is expressed as: $X_{EF} = [(X/Al)_{sample}/(X/Al)_{PAAS}]$. In this equation, X_{EF} represents the enrichment factor for a specific redox sensitive metal, where X is the concentration of that metal and Al is the concentration of aluminum. We then standardize these sample concentrations against the Post-Archean Australian Shale (PAAS) composition, as defined by (Taylor and McLennan, 1995). Enrichment factors exceeding 3 are interpreted as indicative of detectable trace metal enrichment above crustal values, while factors surpassing 10 signify substantial sedimentary enrichment (Algeo and Tribovillard, 2009). In addition to absolute concentrations, we also report carbonate-corrected trace metal concentrations to account for potential dilution effects in carbonate-rich samples. However, the carbonate-correction does not substantially alter the overall stratigraphic trends in the absolute trace metal data.

4. Results

4.1. Abbott River section

The Mulde CIE was first identified within the Cape Phillips Formation, by Noble et al. (2005, 2012) at the Abbott River section. This outcrop is interpreted to have been deposited closer to the basin margin, where it spans from just prior to the *C. lundgreni* Event through the *C. praedeubeli–C. deubeli* biozones and is characterized by a dual-peaked positive excursion, with the first peak reaching +3.4 ‰ magnitude shift, and the second peak following shortly after (Fig. 2A). Pyrite sulfur isotope ($\delta^{34}S_{pyr}$) values fluctuate around 26 ‰, reaching approximately 36 ‰ during the first peak of the Mulde CIE. Subsequently, $\delta^{34}S_{pyr}$ values decrease slightly to ~30 ‰ and then increase again to approximately 40 ‰ prior to the second peak of the Mulde CIE. Following this, $\delta^{34}S_{pyr}$ values show some variability but generally are lowered to values near 25 ‰ (Fig. 2C). Pyrite content is generally below 1 wt%, ranging from near zero to 1.2 wt%, with an average of 0.4 wt% (Fig. 2D).

Iron speciation (Fe_{HR}/Fe_T) for Abbott River are predominantly above 0.38, the threshold for anoxic bottom waters, with only two samples falling below this threshold and one sample below 0.22 (Fig. 3A). Fe_{pyr}/Fe_{HR} ratios for all samples except one are below 0.6, within the threshold for ferruginous bottom waters (Fig. 3B). Fe_T/Al ratios are mostly below 0.55 ± 0.11, the Phanerozoic average shale value (Raiswell et al., 2018), during the *C. lundgreni* biozone but after the extinction horizon showing higher values through the *C. praedeubeli – C. deubeli* biozone but decreased through the L. *progenitor* biozone of the Gorstian (Fig. 3C). Carbonate-corrected trace metal concentrations show the following distributions: Mn (Mn_{CC}) averages 505 ppm (range: 217–1732 ppm) (Fig. 3D), V (V_{CC}) averages 339.6 ppm (range: 56.2–1311.2 ppm) (Fig. 3E), and Mo (Mo_{CC}) averages 25 ppm (range: 5–85 ppm) (Fig. 3F). Vanadium concentrations display a distinct stratigraphic pattern, beginning at moderate levels of ~300–400 ppm in the *C. lundgreni* biozone, then showing significant enrichment up to 1311 ppm coinciding with the early phase of the *lundgreni* extinction event. These elevated V concentrations then decrease markedly through the first peak of the Mulde CIE, dropping to values closer to 56 ppm. Molybdenum exhibits a parallel trend, with concentrations increasing to maximum values of about 85 ppm during the early extinction interval, followed by a notable decrease to approximately 5–10 ppm during the peak of the Mulde CIE. TOC normalized values of Mo predominantly follow the trends of Mo_{CC} concentrations with the highest value of 107 ppm at the end of the *C. lundgreni* biozone (extinction event interval) (Fig. 3F).

4.2. Twilight Creek Section

The Mulde CIE has also been documented in the more distal setting of the Twilight Creek section (Fig. 4) (Noble et al., 2012). Pyrite sulfur isotope ($\delta^{34}S_{pyr}$) values exhibit some variability throughout the upper Sheinwoodian, with average values being around 28 ‰. At the end of the lower Homerian, values are approximately 25 ‰, increasing to around 31 ‰ at the lower/upper Homerian boundary (coincident with the first peak of the Mulde CIE). $\delta^{34}S_{pyr}$ values then show a decreasing trend before the early Gorstian, where they increase again to approximately 32 ‰ before decreasing (Fig. 4C). Pyrite content is consistently below 1 wt%, ranging from near zero to 0.7 wt%, with an average of 0.2 wt% (Fig. 4D).

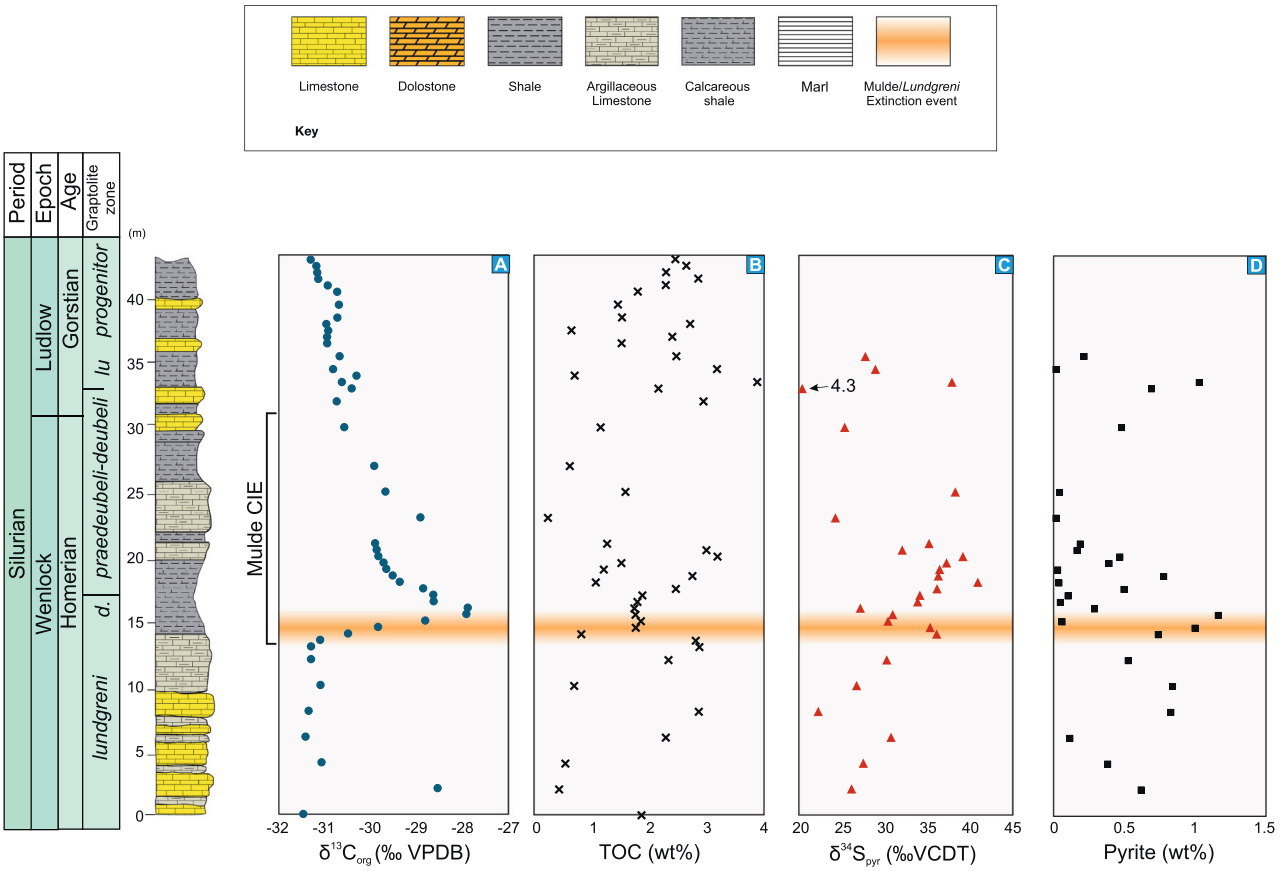

Fig. 2. Stratigraphic profiles from the Abbott River section showing A) Organic carbon isotope ($\delta^{13}C_{org}$) data, B) total organic carbon (TOC, wt%), C) Pyrite sulfur isotope ($\delta^{34}S_{pyr}$) data, and D) pyrite contents (wt%). The orange bar marks the interval corresponding to the Mulde/*lundgreni* extinction horizon. The black arrow indicates isolated data points discussed in the text. $\delta^{13}C_{org}$ and TOC data replotted from (Noble et al., 2012). Graptolite biozone abbreviations used in this study are *d.* = *Pristiograptus dubius* – *Gothograptus nassa* Zones, and *lu.* = *Colonograptus ludensis* biozones.

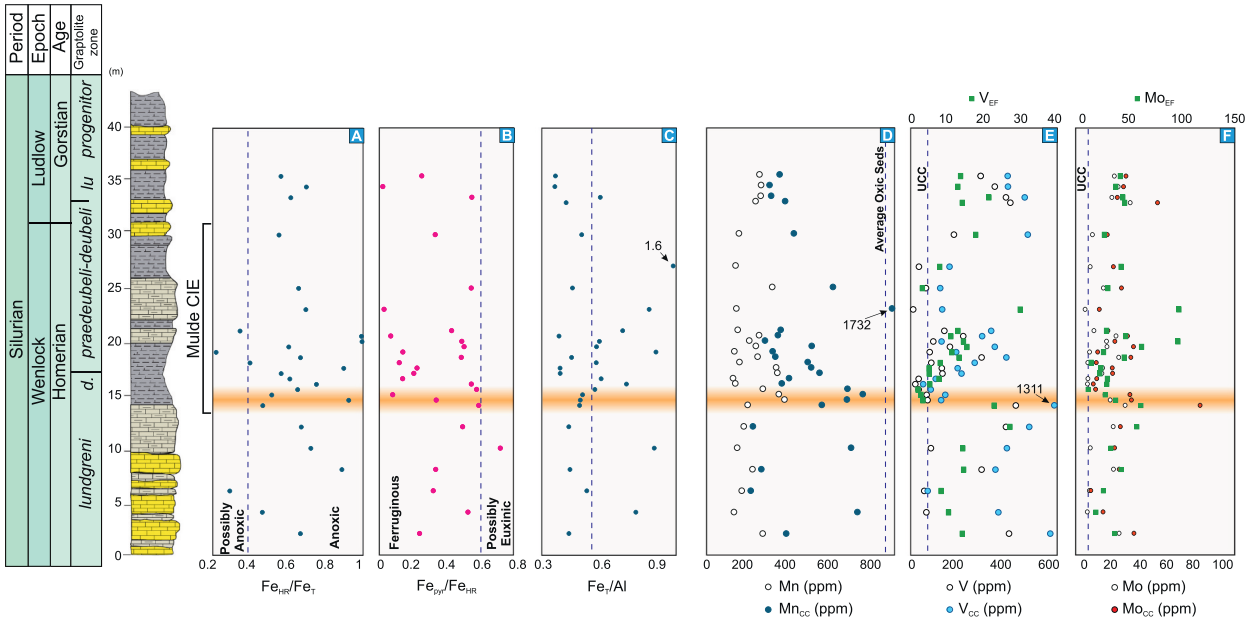

Fig. 3. Iron speciation and trace metal data from the Abbott River section. A) Ratios of highly reactive iron to total iron (Fe_{HR}/Fe_T). B) Ratios of pyrite iron to highly reactive iron (Fe_{pyr}/Fe_{HR}). C) Total iron to aluminum ratios (Fe_T/Al). D-F) Absolute and carbonate-corrected concentrations of manganese (Mn), vanadium (V), and molybdenum (Mo), respectively, as well as enrichment factors (EF) for V and Mo. The orange bar marks the interval corresponding to the Mulde/*lundgreni* extinction horizon. UCC = upper continental crust; CC = carbonate-corrected. The black arrow indicates isolated data points discussed in the text.

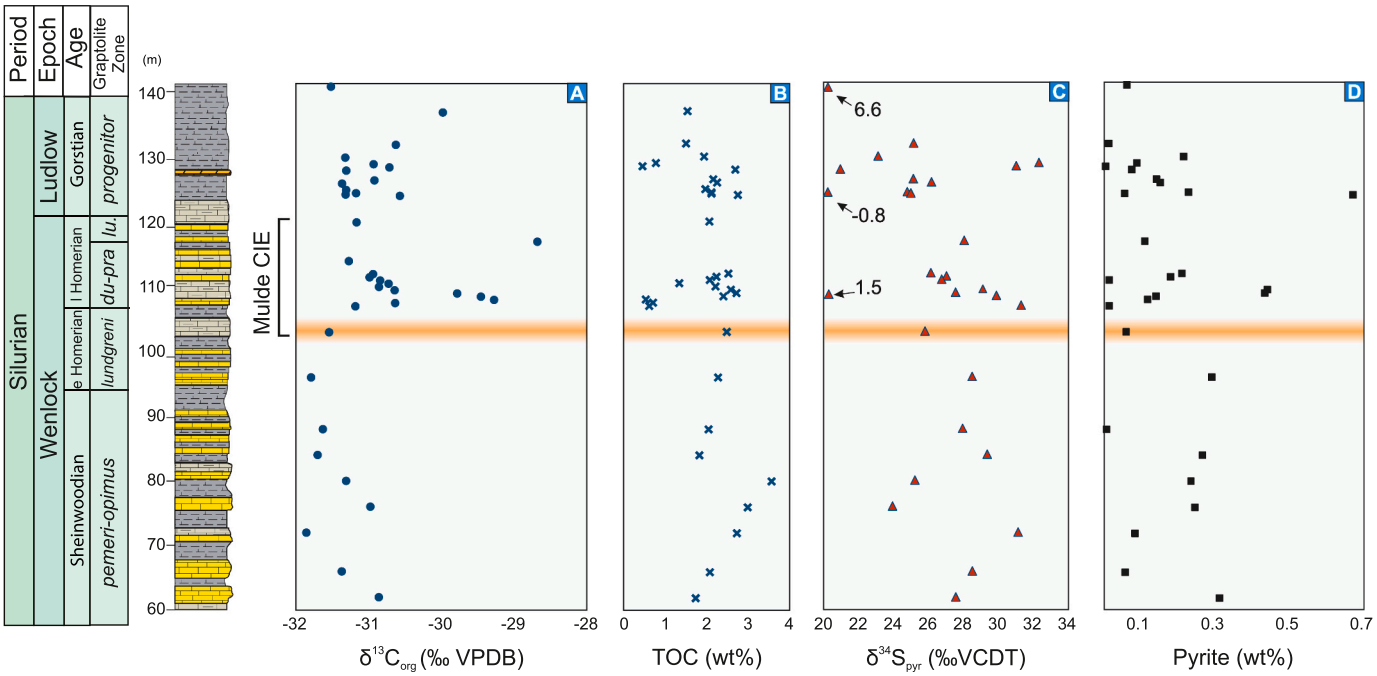

Fig. 4. Stratigraphic profiles from the Twilight Creek section showing A) Organic carbon isotope ($\delta^{13}C_{org}$) data, B) total organic carbon (TOC, wt%), C) Pyrite sulfur isotope ($\delta^{34}S_{pyr}$) data, and D) pyrite contents (wt%). The orange bar marks the interval corresponding to the Mulde/*lundgreni* extinction horizon. The black arrow indicates isolated data points discussed in the text. $\delta^{13}C_{org}$ and TOC data replotted from (Noble et al., 2012).

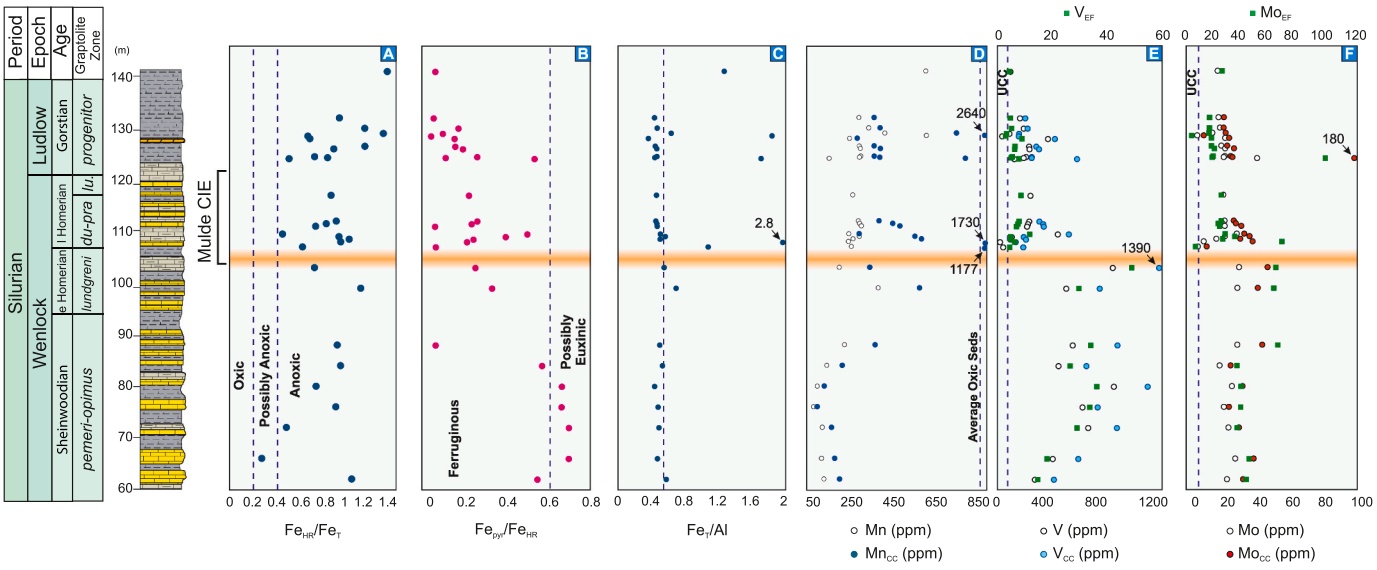

Fig. 5. Iron speciation and trace metal data from the Twilight Creek section. A) Ratios of highly reactive iron to total iron (Fe_{HR}/Fe_T). B) Ratios of pyrite iron to highly reactive iron (Fe_{pyr}/Fe_{HR}). C) Total iron to aluminum ratios (Fe_T/Al). D-F) Absolute and carbonate-corrected concentrations of manganese (Mn), vanadium (V), and molybdenum (Mo), respectively, as well as enrichment factors (EF) for V and Mo. The orange bar marks the interval corresponding to the Mulde/*lundgreni* extinction horizon. UCC = upper continental crust; CC = carbonate-corrected. The black arrow indicates isolated data points discussed in the text.

Fe speciation data show Fe_{HR}/Fe_T ratios exceeding 0.38 for all samples except one, above the anoxic threshold, from the upper Sheinwoodian which falls within the possibly anoxic interval of 0.38 to 0.22 (Fig. 5A). Fe_{pyr}/Fe_{HR} ratios predominantly fall below 0.6, falling within the ferruginous range, with some Sheinwoodian samples ranging between 0.6 and 0.8 within the possibly euxinic range (Fig. 5B). Fe_T/Al ratios are predominantly close to the Phanerozoic average shale value near 0.55 ± 0.11. Interestingly coincident with the first peak of the Mulde CIE two Fe_T/Al values rise significantly above 0.55, in addition to a few points within the Gorstian part of the section (Fig. 5C).

Carbonate-corrected trace element concentrations show the following distributions: Mn concentrations were low, averaging 551.7 ppm (range: 112.3–2640.6 ppm) (Fig. 5D); V concentrations were high, averaging 460.3 ppm (range: 134.2–1390.6 ppm) (Fig. 5E); and Mo concentrations were elevated, averaging 31.4 ppm (range: 5.2–180.3 ppm) (Fig. 5F). Vanadium concentrations exhibit a pronounced stratigraphic trend, beginning at relatively high levels around 600–700 ppm in the Sheinwoodian, then progressively increasing to reach peak enrichments of approximately 1391 ppm just before the *lundgreni* extinction interval. Following this maximum enrichment, V concentrations

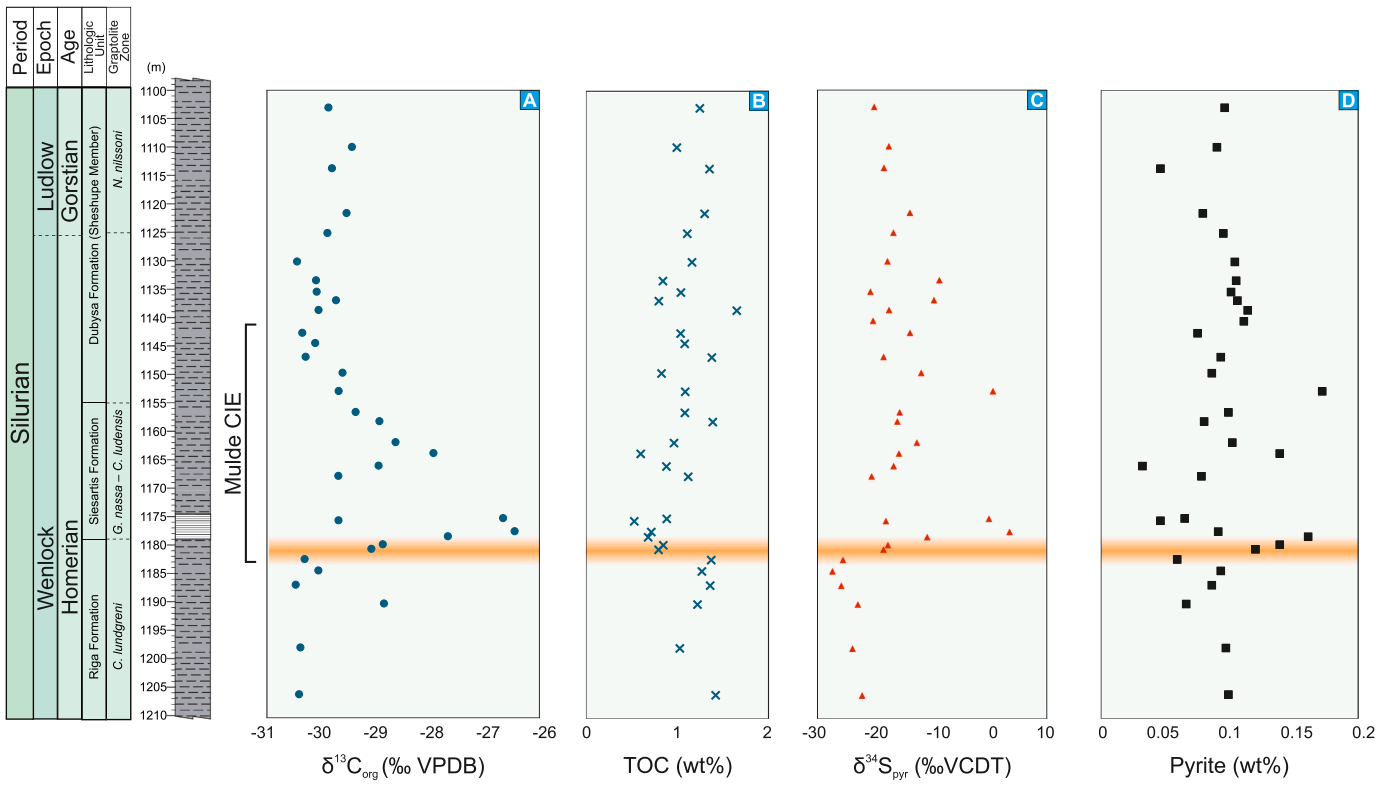

Fig. 6. Stratigraphic profiles from the Priekule-20 core showing A) Organic carbon isotope ($\delta^{13}C_{org}$) data, B) total organic carbon (TOC, wt%), C) Pyrite sulfur isotope ($\delta^{34}S_{pyr}$) data, and D) pyrite contents (wt%). The orange bar marks the interval corresponding to the Mulde/*lundgreni* extinction horizon.

decrease substantially through the first peak of the Mulde CIE, declining to values around 134 ppm in the upper Homerian. Molybdenum demonstrates a similar pattern through this interval, with concentrations increasing to about 40–50 ppm leading into the extinction event, followed by a marked decrease to approximately 5 ppm during the Mulde CIE interval. Both elements show some enrichment in the early Gorstian,

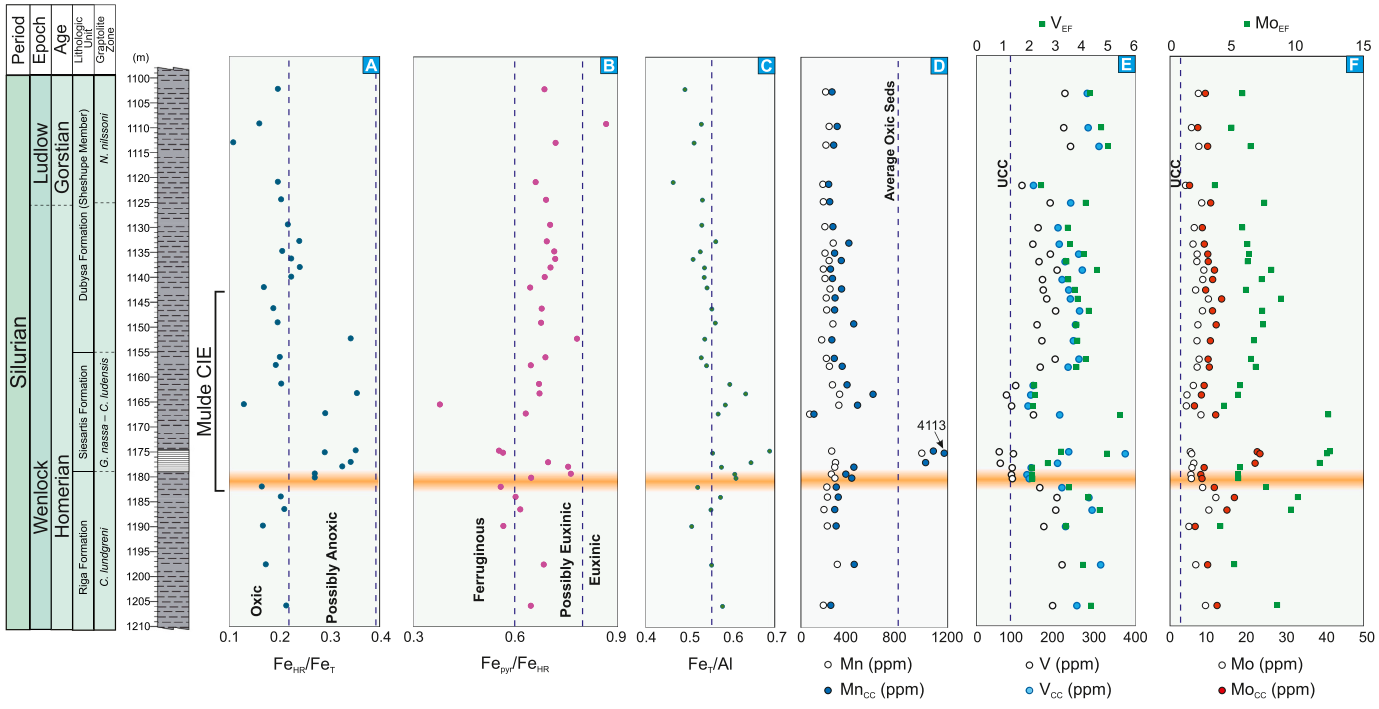

Fig. 7. Iron speciation and trace metal data from the Priekule-20 core. A) Ratios of highly reactive iron to total iron (Fe_{HR}/Fe_T). B) Ratios of pyrite iron to highly reactive iron (Fe_{pyr}/Fe_{HR}). C) Total iron to aluminum ratios (Fe_T/Al). D-F) Absolute and carbonate-corrected concentrations of manganese (Mn), vanadium (V), and molybdenum (Mo), respectively, as well as enrichment factors (EF) for V and Mo. The orange bar marks the interval corresponding to the Mulde/*lundgreni* extinction horizon. UCC = upper continental crust; CC = carbonate-corrected. The black arrow indicates isolated data points discussed in the text.

with V reaching around 800 ppm and Mo showing elevated values, before returning to lower concentrations. TOC normalized values of Mo track the trends of Mo_{CC} concentrations with peaks of 65 during the first peak of the Mulde CIE and within the Gorstian (Fig. 5F).

4.3. Priekule-20 core

The Mulde CIE recorded within the Priekule-20 core exhibits the double-peaked pattern recorded in other sections globally, with the first peak in $\delta^{13}C_{org}$ having a maximum magnitude of +3.65 ‰. The first peak occurs after the *Cyrtograptus lundgreni* and *Gothograptus nassa–Colonograptus ludensis* graptolite biozone boundary (coinciding with the Riga and Siesartis formational boundary), while the second peak is within the *G. nassa-C. ludensis* biozone (Fig. 6A). Total organic carbon (TOC) content averages 1.1 wt%, ranging from 0.5 to 1.7 wt% (Fig. 6B). Pyrite sulfur isotope ($\delta^{34}S_{pyr}$) values fluctuate around −22 ‰ in the *C. lundgreni* biozone, then abruptly increase across the *C. lundgreni* and *G. nassa-C. ludensis* graptolite biozones boundary, reaching +3.4 ‰ at the peak of the CIE (early *G. nassa-C. ludensis* biozones). Subsequently, values decrease and fluctuate between −20 ‰ and − 10 ‰, with an exception of a positive value of 0.5 ‰ at the Siesartis and Dubysa Formations boundary (Fig. 6C). Pyrite content is uniformly low, ranging from 0.03 to 0.2 wt%, with an average of 0.1 wt% (Fig. 6D).

Fe speciation data show Fe_{HR}/Fe_T ratios below 0.22 for all samples in the *C. lundgreni* graptolite biozone, within the oxic range. Values range between 0.22 and 0.38, within the possibly anoxic range, from the lower part of the *G. nassa-C. ludensis* biozones (first peak of the Mulde CIE) through the lower part of the Siesartis Formation. For the remainder of the section, most of the Fe_{HR}/Fe_T values fluctuate near 0.22 (Fig. 7A). Fe_{pyr}/Fe_{HR} ratios for most samples range between 0.6 and 0.8, within the possibly euxinic bottom waters range, with a few samples below 0.6 and one approximately 0.8 (Fig. 7B). Fe_T/Al ratios ranged from 0.46 to 0.69. However, Fe_T/Al ratios were elevated above the Phanerozoic average shale value of 0.55 within the Mulde CIE interval (Fig. 7C).

Carbonate-corrected trace element concentrations show the following distributions: Mn concentrations were low, averaging 325.2 ppm (range: 95.8–1295.8 ppm) (Fig. 7D); V concentrations were modestly elevated, averaging 198.6 ppm (range: 70.6–308.6 ppm) (Fig. 7E); and Mo concentrations were low, averaging 9.1 ppm (range: 5.3–15.5 ppm) (Fig. 7F). Vanadium concentrations show modest enrichments beyond UCC values, around 250–300 ppm in the *C. lundgreni* biozone, then increasing to reach maximum enrichments of approximately 308.6 ppm near the *lundgreni* extinction horizon and the boundary between the Riga and Siesartis Formations. Following this enrichment, V concentrations decline notably through the first peak of the Mulde CIE, dropping to values around 100 ppm in the *G. nassa-C. ludensis* graptolite biozones. Molybdenum exhibits a similar temporal trend, albeit with more modest absolute values, increasing from baseline values of around 8–10 ppm to reach enrichments of ~16 ppm leading into the extinction interval, followed by a decrease to approximately 6–7 ppm during the Mulde CIE, with a subtle recovery to values of 8–10 ppm afterward. Both V and Mo maintain relatively stable concentrations through the remainder of the studied interval, with only minor fluctuations in the upper part of the core succession. TOC normalized values of Mo range from 4 to 14 and broadly track the trends in Mo_{CC} data.

5. Discussion

Although the majority of our samples are fine-grained siliciclastic shales, some intervals display elevated carbonate contents. Following (Clarkson et al., 2014), we applied a minimum threshold of >0.5 wt% total Fe to ensure reliable redox interpretations in these carbonate-rich samples. Almost all of our samples exceeded the Fe_T threshold, with only three exceptions. We have identified coincident positive excursions in both $\delta^{13}C_{org}$ and $\delta^{34}S_{pyr}$ records from all three successions, indicating that in both of these marine basins recorded evidence of enhanced burial of pyrite and organic matter during the first peak of the Mulde CIE. Changes in sedimentary $\delta^{34}S_{pyr}$ values are interpreted to reflect local sulfur cycling changes or possibly reflect early-stage diagenetic processes (Pasquier et al., 2017). $\delta^{34}S_{pyr}$ values can be influenced by several local factors such as sedimentation rates, types of organic matter, and local oxygen penetration depths (Gomes and Hurtgen, 2015), and it is very unlikely that these disparate basins would have the same depositional and post-depositional histories, given the differences in hydrographic settings and respective continental margins (Panthalassic vs. Rheic oceans). Therefore, the similar trends in $\delta^{13}C_{org}$ and $\delta^{34}S_{pyr}$ (i.e., nearly coincident positive shifts) suggest that both of these records could reflect changes in the global pyrite and organic carbon burial rates, rather than local processes. Even though we cannot rule out diagenetic processes and local influences entirely, these processes seem minimal as secondary factors (amplifying or dampening magnitudes) and thus we evaluate our paleoredox proxy datasets as being mostly reflective of primary seawater conditions. Here we will first discuss our iron geochemistry, sulfur isotopes, and trace metal concentrations within the context of local paleoredox conditions within the Franklinian shelf and Baltoscandian paleobasin, respectively. Subsequently, with local paleoredox conditions constrained in both paleobasins, we then interpret changes in V, Mo, and U concentrations and $\delta^{34}S_{pyr}$ to possibly reflect changes within the global extent of reducing conditions in mid-Silurian oceans. Finally, these combined local, and possibly global, perspectives on marine (de)oxygenation will be linked to well-established mid-Silurian biodiversity trends.

5.1. Local redox conditions in the deep shelf/slope of northern Laurentia

Iron speciation indicates that at both northern Laurentian sections (Abbott River and Twilight Creek; Figs. 3 and 5) there were persistently reducing marine bottom water conditions, with almost all Fe_{HR}/Fe_T values above the 0.38 anoxic threshold. Most of the Fe_{pyr}/Fe_{HR} values from both Laurentian sections are below the 0.6 threshold for possibly euxinic conditions, and when taken together with the corresponding Fe_{HR}/Fe_T data we can interpret this portion of the Franklinian deep shelf/slope had persistently ferruginous-anoxic bottom waters throughout this interval of the mid-Silurian. Fe_T/Al ratios in the Abbott River section are generally close to the Phanerozoic average shale values ($Fe_T/Al = 0.55 \pm 0.11$; Raiswell et al., 2018) before the extinction horizon, indicating a predominantly detrital Fe source with limited redox-driven Fe mobilization. Some variability is observed in the Fe_T/Al data with lower values ($Fe_T/Al < 0.55 \pm 0.11$) possibly reflecting higher sedimentation rates, which can suppress Fe enrichment by diluting Fe accumulations in the sediment (Raiswell et al., 2018). During the Mulde CIE, Fe_T/Al values are mostly enriched beyond the Phanerozoic average shale ($Fe_T/Al > 0.55 \pm 0.11$), suggesting benthic Fe shuttling and Fe remobilization under reducing conditions (Hardisty et al., 2018). These trends point to periodic Fe transport and redeposition, likely driven by fluctuating redox conditions rather than changes in detrital input. In the Twilight Creek section, Fe_T/Al values remain close to Phanerozoic average shale values for much of the interval, but show similar enrichments within the Mulde CIE, as seen in Abbott River section, suggesting localized Fe mobilization and redox-driven Fe cycling (Hardisty et al., 2018). However, the higher Fe_T/Al values during the Mulde CIE likely indicates some benthic Fe shuttling processes, where enhanced Fe redeposition occurred reflecting an active iron shuttle in the basin at this time (Raiswell et al., 2018). These patterns further support our corresponding iron speciation data of persistently ferruginous conditions, with Fe cycling playing a key role in local geochemical trends.

Manganese (Mn) concentrations of analyzed samples from the Abbott River and Twilight Creek sections exhibit values below the average Mn concentration of modern oxic sediments (~850 ppm; (Morford and Emerson, 1999). Even after carbonate correction, only a limited number of samples exceed this threshold (Figs. 3 and 5), broadly supporting the Fe speciation data that indicate locally reducing

conditions (Boyer et al., 2011). Vanadium (V) concentrations show a distinct stratigraphic pattern in both sections, beginning at moderate levels of ~300–400 ppm in the *C. lundgreni* Zone, then showing significant enrichment up to 1311 ppm (Abbott River) and 1391 ppm (Twilight Creek) coinciding with the early phase of the *lundgreni* extinction event. These elevated V concentrations then decrease markedly through the first peak of the Mulde CIE, dropping to values closer to upper continental crust levels (UCC, 97 ppm) in both sections. Vanadium requires local water columns to be suboxic to anoxic to become enriched within the sediments, but not necessarily euxinic conditions (Algeo and Maynard, 2004; Owens et al., 2016, 2017). In severely reducing conditions (e.g., euxinic bottom waters) V can be enriched to concentrations of many hundreds to thousands of ppm (Young et al., 2020; Bowman et al., 2021; Kozik et al., 2023). This pattern of initial enrichment followed by depletion suggests significant changes in local redox conditions – from strongly reducing environments that enabled substantial V accumulation in sediments prior to and during the early extinction interval, to conditions that limited V sequestration during the first peak of the CIE.

Molybdenum concentrations exhibit similar trends to V in both sections, increasing to ~40–50 ppm at Twilight Creek and ~ 85 ppm at Abbott River during the early extinction interval, followed by a notable decrease to ~5–10 ppm during the first peak of the Mulde CIE. The moderate Mo enrichments (20–40 ppm) throughout most of both sections suggest at least sulfidic pore waters underlying anoxic bottom waters. However, it is possible that some intervals of intermittent water column euxinia existed (Scott and Lyons, 2012; Hardisty et al., 2018). Given the local redox conditions were stable, based on the Fe speciation and [Mn], the subsequent decrease in Mo concentrations could be indicative of a drawdown in the oceanic Mo reservoir due to globally extensive reducing/euxinic conditions can lead to a global depletion of dissolved Mo (Algeo, 2004; Owens et al., 2016). Alternatively, this could reflect a local change in the bottom water redox conditions from strongly reducing to reducing (e.g., non-sulfidic but still anoxic).

Cross-plots of U and Mo enrichment factors (U_{EF} vs Mo_{EF}) can provide valuable insights into paleoceanographic conditions, including benthic redox states, the degree of basin restriction, and the evolution of water mass chemistry during deposition (Algeo and Tribovillard, 2009) (Fig. 8). Almost all of the samples at the Abbott River and Twilight Creek sections record enrichment of >10 for both U_{EF} and Mo_{EF} with just a few samples showing U_{EF} below 10 (Fig. 8), plotting mostly near the 0.3 × seawater (SW) line. However, six samples record Mo_{EF} values above the 1 × SW line indicating intervals of strongly reducing, possibly euxinic conditions, potentially with an active particulate shuttle enhancing Mo enrichment (Algeo and Tribovillard, 2009). The generally higher Mo_{EF} values than U_{EF}, averages of 36 and 24, respectively, imply anoxic conditions with Fe reduction zone within the water column, allowing for additional enrichment of Mo and bolstering the interpretations of local redox conditions from Fe speciation as predominantly ferruginous bottom water conditions (Algeo and Tribovillard, 2009). The Mo_{EF}-U_{EF} covariation pattern for both the Abbott River and Twilight Creek sections indicates variable redox from anoxic to possibly euxinic bottom water conditions during deposition.

Mo_{EF}-U_{EF} cross-plots have also been used to interpret basin connectivity through comparison of Mo/U molar ratios with those of open seawater (*c.* 7.5–7.9; Algeo and Tribovillard, 2009). Additionally, [Mo]-TOC cross-plots can be used to interpret basin connectivity by comparison of Mo/TOC ratios with those of modern euxinic basins with varying degrees of restriction to the open ocean (Algeo and Lyons, 2006). The ratios for both Abbott River and Twilight Creek sections fall primarily between 1× and 0.3× the molar ratio of seawater (Fig. 8), indicating that these shales were likely deposited under predominantly anoxic conditions as opposed to euxinic or suboxic. Importantly, the common occurrence of open-marine pelagic graptolite and radiolarian faunas (Noble et al., 2005, 2012) throughout these entire sections indicates good exchange of open marine waters. The wide range of Mo_{EF}-U_{EF} values and the Mo/TOC ratios (Fig. 8) from the northern Laurentia deep shelf/slope that plot above the 1 × SW line to near the 0.3 × SW line indicate redox variation from a largely open marine setting. In summary, our iron and trace metal geochemistry indicate that shales from this region of northern Laurentian were deposited under predominantly ferruginous anoxic conditions in a largely open marine setting during the mid-Homerian.

5.2. Local redox conditions in the deep shelf of Baltica

Iron speciation indicates that the succession from Baltica (Priekule-20 core, Latvia) before and after the Mulde extinction event fall within the oxic range of Fe_{HR}/Fe_T less than 0.22, and throughout the Mulde CIE the Fe_{HR}/Fe_T values range between 0.22 and 0.38, interpreted as possibly anoxic (Fig. 7). The corresponding Fe_{pyr}/Fe_{HR} largely fall within the "possibly euxinic" range (0.6 to 0.8). The Fe_T/Al ratios in the Priekule-20 core are generally close to the Phanerozoic average shale value (Fe_T/Al = 0.55 ± 0.11; Raiswell et al., 2018) before and after the

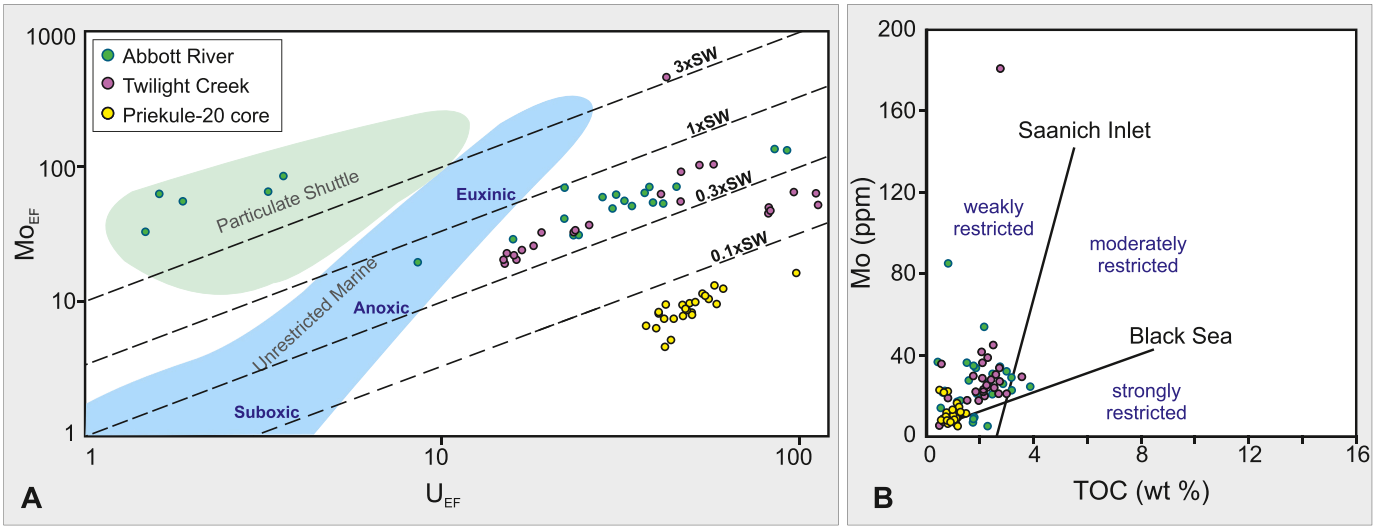

Fig. 8. A) Cross-plot of uranium and molybdenum enrichment factors (U_{EF} vs. Mo_{EF}) from the Abbott River, Twilight Creek, and Priekule-20 core. Dashed lines indicate Mo/U ratios between 7.5 and 7.9 and fractions of seawater (SW) adapted from Algeo and Tribovillard (2009). B) Cross-plot of molybdenum (Mo) versus total organic carbon (TOC) from the same sections, presented in a modified diagram of Algeo and Lyons (2006).

Mulde CIE, suggesting a predominantly detrital Fe source with minimal enrichment. During the Mulde CIE, Fe_T/Al values show significant enrichments beyond the Phanerozoic average indicating benthic Fe shuttling and Fe remobilization under reducing conditions (Hardisty et al., 2018). These coincident Fe enrichments with higher carbon isotope values of the Mulde CIE, suggest a link between enhanced Fe cycling and fluctuating local paleoredox shifts associated with this global carbon cycle perturbation.

Manganese (Mn) concentrations in the Priekule-20 core are consistently low throughout the study interval, most values are <400 ppm, with a few data points near ≥750 ppm (Fig. 7D). The consistently low Mn values, are well below average oxic sediment levels (850 ppm), indicating persistent reducing conditions (e.g., Mn-reduction) and low oxygen availability in this part of the basin. When the persistently low [Mn] are combined with the Fe speciation data suggesting variable redox conditions ranging from possibly oxic to ferruginous throughout the Mulde CIE interval, the most parsimonious interpretation is that bottom waters were reducing throughout but oscillated from being within the Mn-reduction to Fe-reduction portions of the redox ladder. Vanadium concentrations are only modestly enriched beyond UCC values, at ~250–300 ppm in the *C. lundgreni* biozone, reach maximum enrichments of approximately 309 ppm within the extinction horizon, near the boundary between the Riga and Siesartis formations. Subsequently, V decline notably through the first peak of the Mulde CIE, dropping to values around 100 ppm in the *G. nassa–C. ludensis* graptolite biozones. Trends within molybdenum concentrations exhibit a similar pattern to V enrichments in the Priekule-20 core, albeit with only minor to moderate enrichments beyond UCC values, increasing from baseline values of around 8–10 ppm to reach maximum enrichments of 16 ppm within the extinction interval, followed by a decrease to approximately 6–7 ppm during the Mulde CIE, with a subtle recovery to minor–moderate enrichments ~10 ppm afterward. The Mo values are much less enriched compared to the Arctic Canada sections, but interestingly a similar pattern of enrichment and drawdown is observed both in the Priekule-20 core and the Arctic Canada sections. The overall minor enrichments of Mo throughout the Priekule-20 core suggests this deeper shelf setting did not experience significantly reducing conditions (i.e., euxinic conditions) within the bottom waters, but there may have been some intervals of sulfidic conditions that developed only within the sediment porewaters of this part of the basin.

Based upon the calculated values for U and Mo enrichment factors, uranium shows significant enrichments compared to molybdenum throughout these mudstones of the Priekule-20 core. The U_{EF} values range from 28.51 to 102.6, with an average of 44.4, and Mo_{EF} values ranged from 3.5 to 12.4, with an average of 7.1 (Fig. 8). All samples plot below the 0.1 × SW line, indicating predominantly suboxic to anoxic bottom water conditions during deposition. This trend reflects preferential enrichment of U over Mo, likely due to U reduction occurring before significant Mo accumulation. The extremely low Mo/U ratios suggest suboxic to anoxic conditions with minimal sulfide availability or Mo depletion in the water column, likely indicating basin restriction (Algeo and Tribovillard, 2009). These Mo_{EF}-U_{EF} cross-plot and [Mo]-TOC cross-plot patterns (Fig. 8) are consistent with a moderately restricted basin setting characterized by suboxic to anoxic, but not euxinic, bottom waters. In summary, our iron and trace metal geochemistry indicate that shales from this region of Baltica were deposited under suboxic conditions prior to and after the Mulde CIE interval and ferruginous anoxic conditions during the Mulde CIE in a moderately restricted marine setting during the mid-Homerian. The shifts within the iron speciation data combined with variable trace metal concentrations suggest an expansion then contraction of an oxygen minimum zone (OMZ) in the deep shelf of the Baltic Basin during this interval of the Silurian. Interestingly, iron- and trace element-geochemistry have indicated an OMZ expansion followed by contraction within this same basinal setting during the late Silurian Lau/*kozlowskii* event (Bowman et al., 2021).

5.3. Implications for Homerian global redox conditions

This study provides the first shale-based redox proxy data spanning the Homerian Stage and the Mulde/*lundgreni* extinction event and associated CIE. The parallel positive $\delta^{13}C_{org}$ and $\delta^{34}S_{pyr}$ excursions recorded from the Abbott River, Twilight Creek, and Priekule-20 core sections indicate enhanced burial of reduced carbon and sulfur as organic matter, pyrite, and organic sulfur compounds under anoxic to euxinic marine bottom waters (e.g., Gill et al., 2011). The Laurentian sections record a + 15 ‰ to +6 ‰ magnitude shift in $\delta^{34}S_{pyr}$ (Abbott River and Twilight Creek, respectively), while the Priekule-20 core records a + 25 ‰ magnitude shift. The variations in both baseline values and excursion magnitudes of $\delta^{34}S_{pyr}$ reflect distinct characteristics of each depositional setting with regards to microbial sulfur cycling (e.g., local organic matter sources, local redox conditions, iron availability) (Gomes and Hurtgen, 2015). However, the striking synchronicity of these positive shifts across geographically separated regions points to a broader global signal overprinting these local effects. The parallel positive excursions in both $\delta^{13}C_{org}$ and $\delta^{34}S_{pyr}$ across all studied sections indicate enhanced burial of reduced carbon and sulfur as organic matter and pyrite during this interval, suggesting widespread expansion of reducing conditions in the global oceans. When our Homerian $\delta^{13}C_{org}$ and $\delta^{34}S_{pyr}$ excursion records are interpreted with Fe speciation and trace metal datasets they are consistent with a transient increase in global burial rates of reduced carbon and sulfur species.

Trace metal concentrations (i.e., V, U, Mo) can elucidate key aspects of global ocean chemistry through time, including redox state, trace metal availability, and fluctuations in marine reservoir size. Interestingly the strongest enrichments are found within our V records, with Mo data recording only minor enrichments but still exhibiting similar patterns enrichment to vanadium (Figs. 3, 5, 7). The remarkably coincident nature of the trends in trace metal datasets, recording two distinct intervals of enrichment followed by declining concentrations in all three sections from two different ocean basins, argues against purely local factors (e.g., changes in local redox, changes in hydrographic connectivity) driving these trends. Importantly, recently published trace metal records from the Prague Basin (peri-Gondwana terrane; Perunica) show the same temporal pattern of initial enrichment followed by drawdown (Frýda and Frýdová, 2025), further supporting the interpretation that these patterns reflect global changes in seawater inventories of these trace metals. The overall lower trace metal concentrations from the deep shelf of Baltica as compared to the deep shelf/slope setting of northern Laurentia reflect local/basin scale marine redox differences, however the coincident trends in trace metal datasets are still recorded in all successions. Collectively, when all of these Homerian trace metal datasets from three different paleocean basins are combined they strongly suggest a fluctuations in the global marine inventories of these trace metals during this interval of the mid-Silurian. The initial trace metal enrichments (V, Mo) in the early Homerian followed by drawdown into the first peak of the Mulde CIE, initially reflect a sufficiently large global reservoir of these elements to allow for such local enrichments but subsequently these reservoirs became drawn down at a global scale coinciding with the interval of extinction. This interpretation suggests that throughout this interval of the early Homerian anoxic marine conditions became more widespread or sufficiently reducing (i.e., euxinic) at global scales to induce a reservoir drawdown (Lyons et al., 2009; Reinhard et al., 2013; Owens et al., 2016; Kozik et al., 2023). Following the first peak of the Mulde CIE trace metal records from all sections record enrichments beyond UCC values in the mid-Homerian (Fig. 9), suggesting redox conditions within the oceans became less reducing and/or the extent of anoxic bottom waters contracted to allow for trace metal inventories to increase enough for local enrichments again. This second interval of trace metal enrichment was followed by another interval of drawdown that corresponds to the second peak of the Mulde CIE suggesting a second interval of expanded anoxic marine conditions in the late Homerian.

Dramatic declines in trace metal concentrations have been associated with Late Cretaceous OAE2 with V being drawn down prior to the CIE and Mo drawdown coincident with the CIE (Owens et al., 2016, 2017). Of note, model estimates suggest that only 3 to 7 % of the seafloor experienced very reducing (i.e., euxinic) conditions during OAE2. Thus, global ocean-scale reducing conditions are not necessary for these trace metal drawdown events (Owens et al., 2016; Dickson et al., 2017), although a greater extent of reducing conditions is required if there is less euxinia globally. While local redox conditions in our study areas do not indicate stable oxic conditions prior to the Mulde CIE, our data indicate, at the very least, two marine regions of expansion of reducing conditions followed by a modest contraction of those reducing marine bottom waters. This pattern of expansion of marine reducing conditions has been recently documented for two Silurian extinction events and associated CIEs (Young et al., 2020; Allman et al., 2024), for the late Cambrian SPICE and associated biomere extinction (Gill et al., 2021), and the Late Ordovician mass extinction and CIE (Zou et al., 2018). In order to confidently attribute our Homerian trace metal patterns of two successive intervals of enrichment–drawdown to either global changes in marine inventories or local basinal factors related to eustatic sea level and open ocean connectivity, further studies at higher resolution sampling are required from sites that are persistently euxinic before, during, and after the Mulde CIE.

5.4. Biotic response (Mulde/lundgreni event) to widespread anoxia

Global palaeobiological records throughout the upper Wenlock (Homerian Stage) document a major marine extinction in the mid-Silurian oceans, with a loss of as many as 95 % of graptolite species in some regions (Štorch, 1995; Lenz et al., 2006; Cooper et al., 2012). The '*lundgreni* Event', while it was the most severe for graptolites, also significantly impacted other planktonic marine groups. Other major phytoplankton and zooplankton groups showed significant reductions in biodiversity, with ~50 % loss of acritarchs, prasinophytes, and ~ 75 % loss of radiolarians (Kaljo et al., 1996; Porębska et al., 2004). Based on chitinozoan records from Baltica, this marine microfossil group also experienced a rapid decline in this interval, with the highest extinction and turnover rates per million year through the entire Ordovician and Silurian (Hints et al., 2018). Conodonts, on the other hand experienced a more modest extinction, the 'Mulde Event', that was stepwise with 3 separate extinction horizons (Jeppsson and Calner, 2002; Jeppsson and Calner, 2002; Porębska et al., 2004; Calner et al., 2006). The extinction event also impacted trilobites, resulting in the global disappearance of multiple genera (Adrain and Edgecombe, 1997). These biotic records have been well integrated with $\delta^{13}C$ records from Perunica, Baltica, and Laurentia (Cramer et al., 2012; Manda et al., 2019; Biebesheimer et al., 2021). Our new data when combined with these previous observations indicate that these marine groups were most likely affected by the same event that caused the perturbations to the global carbon cycle and trace metal inventories. A major biogeochemical perturbation occurred during this time interval and is possibly linked to major climatic feedbacks.

Silurian paleobiological records clearly show major marine faunal turnovers occurred in the mid-Homerian coincident with positive shifts in $\delta^{13}C$ and $\delta^{34}S_{pyr}$ records (Fig. 9). The first peak of the Mulde CIE is associated with increased reducing conditions in marine settings under which carbon and sulfur burial rates likely increased. Marine taxa from planktonic/nektonic to hemipelagic marine groups were specifically most affected in this extinction event, with shallow water sessile epifaunal groups only very marginally impacted. This pattern of extinction broadly coincides with a sea-level drop in the mid-Homerian (Danielsen et al., 2019; Manda et al., 2019) and new geochemical evidence presented here of widespread reducing conditions in these deeper marine settings. Specifically, trace metal data (V, U, Mo) from three different paleocean basins suggest more oxic bottom waters globally, largely predating the extinction event and Mulde CIE as eustatic sea level began to drop. Shale redox proxies from multiple global locations (trace metal drawdowns, positive $\delta^{34}S_{pyr}$) suggest expansion of local and possibly global anoxia during the extinction interval, as sea level was at its lowest and then began to rise during the first peak of the Mulde CIE. Marine biodiversity levels began to recover after the first peak of the Mulde CIE (e.g., Cramer et al., 2012), and trace metal records (V, Mo enrichments) suggest that the extent of the anoxic seafloor contracted while sea level was at a highstand. Shale proxy records (trace metal drawdowns) also indicate another interval of expansion of anoxia

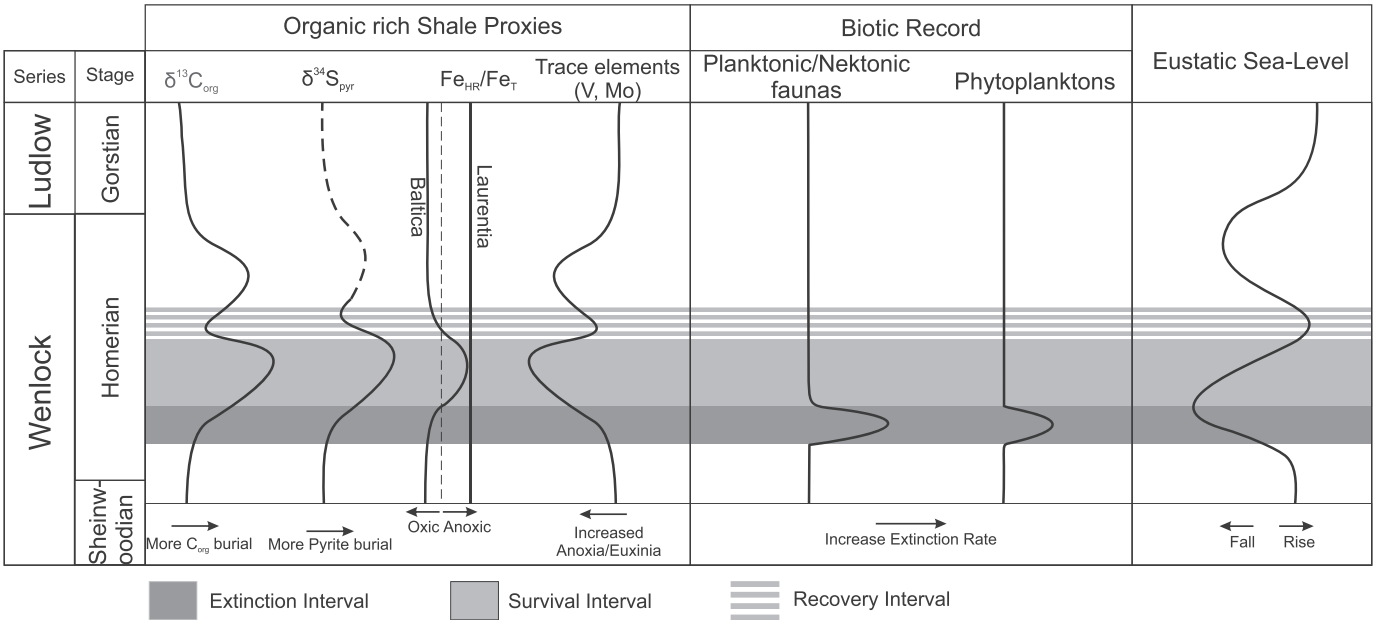

Fig. 9. Geochemical proxies and biotic patterns during the Mulde extinction event. Stratigraphic profiles showing carbon isotopes ($\delta^{13}C_{org}$), sulfur isotopes ($\delta^{34}S_{pyr}$), iron speciation (Fe_{HR}/Fe_T) from Laurentia and Baltica, and trace elements (V, Mo) from Laurentia, Baltica, and Prague Basin (Frýda and Frýdová, 2025) alongside extinction/recovery trends of planktonic/nektonic organisms and phytoplankton, with corresponding sea-level changes. Dark to light gray intervals represent extinction, survival, and recovery phases. Carbon data from Noble et al. (2012), phytoplankton trends from Cramer et al. (2012), sea-level curve modified from (Danielsen et al., 2019).

coincident with the second peak of the Mulde CIE and sea-level fall (Fig. 9). Upon establishment of post-Mulde CIE baseline $\delta^{13}C$ values during sea-level rise, the shale proxy records suggest redox conditions within the global oceans became less reducing. Sequence stratigraphic evidence for sea-level change and paleobiologic extinction–recovery records, combined with this new geochemical evidence for vacillating marine redox conditions, reinforces the role that anoxia was a potential driver for Mulde/*lundgreni* extinction event (Fig. 9). The apparent connections between sea level, redox conditions and extinction highlight the important role that climate likely had in modulating the expansion and contraction of reducing conditions in the mid-Silurian oceans. The specific correlation of two episodes of sea level fall with new geochemical evidence for expanded reducing conditions also can potentially explain the double-peaked expression of the Mulde CIE.

In the context of other major Silurian biogeochemical events, this mid-Homerian event records a distinctive two-phase pattern in trace metal datasets: initial enrichment followed by a decrease in the enrichment pattern suggests a drawdown during two distinct intervals that coincide with the double-peaked nature of the Mulde CIE. This contrasts with the late Ludlow Lau CIE, which exhibits a single trace metal drawdown phase (Bowman et al., 2021; Allman et al., 2024), suggesting different temporal dynamics in the expansion and contraction of reducing conditions between these Silurian events. Furthermore, the taxonomic selectivity of the Mulde/*lundgreni* extinction differs markedly from the Lau/*kozlowskii* extinction event (e.g., Noble et al., 2012 and references therein). The Mulde/*lundgreni* extinction primarily affected planktonic/hemipelagic taxa, and a more modest stepwise extinction among conodonts, while other benthic taxa remained relatively unaffected. In contrast, the Lau/*kozlowskii* extinction event impacted a broader spectrum of marine taxa across diverse ecological niches, causing significant extinctions in multiple groups including conodonts, acritarchs, brachiopods, and vertebrates (e.g., Bowman et al., 2019 and references therein). This pattern of selective extinction during the Mulde/*lundgreni* extinction event, coupled with our vacillating trace metal data, suggests a more temporally complex and spatially restricted expansion of anoxic water masses that primarily affected offshore mid-water dwelling organisms, rather than the more widespread anoxia that affected deep to shallow water marine environments during the Lau/*kozlowskii* Event. This pattern of redox-driven, taxonomically selective extinction associated with sea-level drop also differs from the late Llandovery–early Wenlock Ireviken extinction event (e.g., Young et al., 2019 and references therein), where expanded euxinia and sea-level rise have been linked to this marine biotic turnover event.

Importantly, our results suggest that a specific combination of environmental factors that include widespread reducing conditions in offshore marine settings coincident with sea-level fall and potential cooling (e.g., Trotter et al., 2016) led to this mid-Homerian extinction event that primarily affected offshore mid-water dwelling organisms. As shallow marine habitat space was reduced and OMZs expanded, these reducing waters would have been largely confined to deep shelf/ upper slope settings due to coincident sea-level fall (Fig. 9). In this scenario, ferruginous and/or euxinic conditions would have expanded into offshore mid-water depths and disproportionally affected planktonic/ hemipelagic taxa in deeper water settings that are thought to have been more vulnerable to environmental changes (e.g., impacting graptolites; Cooper et al., 2012; Crampton et al., 2016). A similar combination of redox fluctuations, climate variability, and sea-level change has also been implicated in the Late Ordovician Mass Extinction (Kozik et al., 2022a, 2022b). Ultimately, more detailed paleoredox investigations utilizing different proxies ($\delta^{98}Mo$, $\delta^{238}U$, $\varepsilon^{205}Tl$) with different redox sensitivities are needed to gain better insights into the role marine oxygen played in this mid-Homerian event. Additionally, a more thorough investigation and integration of sequence stratigraphy with silicate weathering proxy and sea surface temperature proxy datasets is needed to reconcile the apparent offsets between weathering, climate and sea level responses during this interval of the Silurian (e.g., Johnson, 2010; Trotter et al., 2016; Sproson et al., 2022).

6. Conclusions

The multiproxy geochemical data from the Abbott River, Twilight Creek, and Priekule-20 core sections provide new insights into marine redox dynamics across the Mulde/*lundgreni* extinction event. Our $\delta^{34}S_{pyr}$ records show positive excursions that parallel the first peak of the Mulde CIE, indicating increased pyrite burial under widespread reducing conditions in the mid-Silurian oceans. Iron speciation data reveal basin-specific redox conditions: persistent anoxic-ferruginous bottom waters along the Laurentian margin contrasted with more variable redox conditions within the Baltoscandian basin, that shifted from oxic to anoxic bottom waters during the Mulde CIE. Trace metal concentrations show a distinctive pattern across both paleocontinents – initial enrichment prior to the extinction event followed by significant drawdown during the extinction interval and rising limb of the first peak of the Mulde CIE, suggesting a possibly global expansion of reducing seafloor environments. Subsequently, trace metal concentrations show another interval of enrichment coinciding with the falling limb of the first peak of the Mulde CIE and the biotic recovery interval. This is followed by a second drawdown in trace metal concentrations that coincides with the second peak of the Mulde CIE. This global interpretation and model is further supported by enrichment factors of Mo_{EF} and U_{EF} that indicate varying degrees of basin restriction in both regions; however, similar temporal trends indicate these data while reflecting local factors they also record global signals. The integration of these geochemical datasets provides the first direct evidence linking the Mulde/*lundgreni* biotic crisis with changes in marine redox at both local and potentially global scales.

Contextualizing these geochemical trends with established extinction patterns and eustatic sea-level records, a compelling mechanistic relationship emerges. The synchronous positive excursions in $\delta^{13}C$ and $\delta^{34}S$ coupled with trace metal drawdown suggest that reducing marine conditions expanded across multiple ocean basins during the mid-Homerian, coinciding with the primary extinction pulse of pelagic and hemipelagic fauna and the mid-Homerian sea-level fall. The Silurian oceans demonstrably experienced repeated cycles of coincident sea-level changes, marine extinctions, and perturbations of the global carbon cycle. However, notable differences exist between these marine extinction events and associated positive CIEs (e.g., magnitude, double vs. single peaks), and our data suggest there were differences in cycles of deoxygenation associated with these intervals of the Silurian as well. More broadly, our multiproxy dataset provides further evidence that oxygen levels constituted a major factor controlling Paleozoic biodiversity and evolutionary trajectories, supporting the hypothesis that the Paleozoic Era was characterized by dynamic redox conditions rather than progressive, unidirectional oxygenation of marine environments. The apparent sensitivity of Silurian marine ecosystems to these redox fluctuations highlights the crucial role that ocean oxygen availability played in shaping the evolution of complex marine life throughout the Paleozoic. Meanwhile, the differential responses between taxa during distinct events like the Mulde/*lundgreni* extinction event reveal that extinction selectivity may have been driven by the correspondence of sea level, climate, and intensity of deoxygenation.

CRediT authorship contribution statement

Mahdi Maaleki-Moghadam: Writing – review & editing, Writing – original draft, Visualization, Validation, Software, Resources, Project administration, Methodology, Investigation, Formal analysis, Data curation, Conceptualization. **Anders Lindskog:** Writing – review & editing, Visualization, Validation, Resources, Project administration, Methodology, Investigation, Formal analysis, Data curation. **Paula J. Noble:** Writing – review & editing, Resources, Project administration, Investigation, Funding acquisition, Data curation, Conceptualization.

Dimitri Kaljo: Writing – review & editing, Validation, Resources, Methodology, Investigation, Data curation. **Olle Hints:** Writing – review & editing, Validation, Resources, Investigation, Funding acquisition, Data curation. **John T. Goodin:** Writing – review & editing, Validation, Methodology, Investigation, Formal analysis, Data curation. **Jeremy D. Owens:** Writing – review & editing, Validation, Resources, Project administration, Methodology, Investigation, Funding acquisition, Formal analysis, Data curation, Conceptualization. **Seth A. Young:** Writing – review & editing, Writing – original draft, Validation, Supervision, Resources, Project administration, Methodology, Investigation, Funding acquisition, Formal analysis, Data curation, Conceptualization.

Declaration of competing interest

The authors declare that they have no known competing financial interests or personal relationships that could have appeared to influence the work reported in this paper.

Acknowledgements

Yuxuan Wang and one anonymous reviewer are thanked for their constructive reviews that helped to improve this paper and Alexandre Pohl and Maoyan Zhu for their editorial guidance. We thank Sean Newby, Datu Adiatma, Nevin Kozik, Burt Wolff, and Gary White for their assistance with geochemical analyses at FSU. We thank Charlie Diamond for the assistance with geochemical analyses at UC-Riverside. This work was largely performed at the National High Magnetic Field Laboratory in Tallahassee, Florida which is supported by the National Science Foundation Cooperative Agreement No. DMR-1644779 and by the State of Florida. O.H. acknowledges support from the Estonian Research Council grant PRG1701. This work was supported by the NASA Exobiology Program (80NSSC23K0346 to S.A.Y. and J.D.O.).

Data availability

The authors confirm that all data necessary for supporting the scientific findings of this paper have been provided.

Geochemical and Isotopic Data Across the Silurian Mulde Event from Arctic Canada and Latvia (Original data)

References

Adrain, J.M., Edgecombe, G.D., 1997. Silurian (Wenlock) calymenid trilobites from the Cape Phillips Formation, Central Canadian Arctic. J. Paleontol. 71, 657–682.
Algeo, T.J., 2004. Can marine anoxic events draw down the trace element inventory of seawater? Geology 32, 1057–1060.
Algeo, T.J., Lyons, T.W., 2006. Mo–total organic carbon covariation in modern anoxic marine environments: implications for analysis of paleoredox and paleohydrographic conditions. Paleoceanography 21.
Algeo, T.J., Maynard, J.B., 2004. Trace-element behavior and redox facies in core shales of Upper Pennsylvanian Kansas-type cyclothems. Geochem. Org.-Rich Shales New Perspect. 206, 289–318.
Algeo, T.J., Maynard, J.B., 2008. Trace-metal covariation as a guide to water-mass conditions in ancient anoxic marine environments. Geosphere 4, 872–887.
Algeo, T.J., Tribovillard, N., 2009. Environmental analysis of paleoceanographic systems based on molybdenum–uranium covariation. Chem. Geol. 268, 211–225.
Allman, L.J., Bowman, C.N., Frýda, J., Kozik, N.P., Owens, J.D., Young, S.A., 2024. Constraining reducing conditions in the Prague Basin during the late Silurian Lau/Kozlowskii extinction event. J. Geol. Soc. Lond. 181, jgs2023-108.
Amend, J.P., Edwards, K.J., Lyons, T.W., 2004. Sulfur Biogeochemistry: Past and Present. Geological Society of America.
Anderson, T.F., Raiswell, R., 2004. Sources and mechanisms for the enrichment of highly reactive iron in euxinic Black Sea sediments. Am. J. Sci. 304, 203–233.
Benkovitz, A., Matthews, A., Teutsch, N., Poulton, S.W., Bar-Matthews, M., Almogi-Labin, A., 2020. Tracing water column euxinia in Eastern Mediterranean Sapropels S5 and S7. Chem. Geol. 545, 119627.
Biebesheimer, E.J., Cramer, B.D., Calner, M., Barnett, B.A., Oborny, S.C., Bancroft, A.M., 2021. Asynchronous δ13Ccarb and δ13Corg records during the onset of the Mulde (Silurian) positive carbon isotope excursion from the Altajme core, Gotland, Sweden. Chem. Geol. 576, 120256.
Bowman, C.N., Young, S.A., Kaljo, D., Eriksson, M.E., Them, T.R., Hints, O., Martma, T., Owens, J.D., 2019. Linking the progressive expansion of reducing conditions to a stepwise mass extinction event in the late Silurian oceans. Geology 47, 968–972.
Bowman, C.N., Them II, T.R., Knight, M.D., Kaljo, D., Eriksson, M.E., Hints, O., Martma, T., Owens, J.D., Young, S.A., 2021. A multi-proxy approach to constrain reducing conditions in the Baltic Basin during the late Silurian Lau carbon isotope excursion. Palaeogeogr. Palaeoclimatol. Palaeoecol. 581, 110624.
Boyer, D.L., Owens, J.D., Lyons, T.W., Droser, M.L., 2011. Joining forces: combined biological and geochemical proxies reveal a complex but refined high-resolution palaeo-oxygen history in Devonian epeiric seas. Palaeogeogr. Palaeoclimatol. Palaeoecol. 306, 134–146.
Brüchert, V., Pratt, L.M., 1996. Contemporaneous early diagenetic formation of organic and inorganic sulfur in estuarine sediments from St. Andrew Bay, Florida, USA. Geochim. Cosmochim. Acta 60, 2325–2332.
Calner, M., Kozłowska, A., Masiak, M., Schmitz, B., 2006. A shoreline to deep basin correlation chart for the middle Silurian coupled extinction-stable isotopic event. GFF 128, 79–84.
Calvert, S.E., Pedersen, T.F., 1996. Sedimentary geochemistry of manganese; implications for the environment of formation of manganiferous black shales. Econ. Geol. 91, 36–47.
Canfield, D.E., 2001. Biogeochemistry of sulfur isotopes. Rev. Mineral. Geochem. 43, 607–636.
Canfield, D.E., Raiswell, R., Bottrell, S.H., 1992. The reactivity of sedimentary iron minerals toward sulfide. Am. J. Sci. 292, 659–683.
Clarkson, M.O., Poulton, S.W., Guilbaud, R., Wood, R.A., 2014. Assessing the utility of Fe/Al and Fe-speciation to record water column redox conditions in carbonate-rich sediments. Chem. Geol. 382, 111–122.
Cooper, R.A., Rigby, S., Loydell, D.K., Bates, D.E.B., 2012. Palaeoecology of the Graptoloidea. Earth Sci. Rev. 112, 23–41.
Cramer, B.D., Kleffner, M.A., Saltzman, M.R., 2006. The late Wenlock Mulde positive carbon isotope (δ13Ccarb) excursion in North America. GFF 128, 85–90.
Cramer, B.D., Brett, C.E., Melchin, M.J., Männik, P., Kleffner, M.A., Mclaughlin, P.I., Loydell, D.K., Munnecke, A., Jeppsson, L., Corradini, C., Brunton, F.R., Saltzman, M. R., 2011. Revised correlation of Silurian Provincial Series of North America with global and regional chronostratigraphic units and δ13Ccarb chemostratigraphy. Lethaia 44, 185–202.
Cramer, B.D., Condon, D.J., Soderlund, U., Marshall, C., Worton, G.J., Thomas, A.T., Calner, M., Ray, D.C., Perrier, V., Boomer, I., Patchett, P.J., Jeppsson, L., 2012. U-Pb (zircon) age constraints on the timing and duration of Wenlock (Silurian) paleocommunity collapse and recovery during the "Big Crisis.". Geol. Soc. Am. Bull. 124, 1841–1857.
Crampton, J.S., Cooper, R.A., Sadler, P.M., Foote, M., 2016. Greenhouse-icehouse transition in the late Ordovician marks a step change in extinction regime in the marine plankton. Proc. Natl. Acad. Sci. USA 113, 1498–1503.
Danielsen, E.M., Cramer, B.D., Kleffner, M.A., 2019. Identification of a global sequence boundary within the upper Homerian (Silurian) Mulde Event: high-resolution chronostratigraphic correlation of the midcontinent United States with Sweden and the United Kingdom. Geosphere 15, 839–855.
Dickson, A.J., Gill, B.C., Ruhl, M., Jenkyns, H.C., Porcelli, D., Idiz, E., Lyons, T.W., SHJM, van den Boorn, 2017. Molybdenum-isotope chemostratigraphy and paleoceanography of the Toarcian Oceanic Anoxic Event (early Jurassic). Paleoceanography 32, 813–829.
Frýda, J., Frýdová, B., 2025. High-resolution records of the mid-Homerian (Silurian) marine chemistry evolution and graptolite biodiversity across the Lundgreni Event reveal what nearly killed the graptolites. Palaeogeogr. Palaeoclimatol. Palaeoecol. 668, 112866.
Gill, B.C., Lyons, T.W., Saltzman, M.R., 2007. Parallel, high-resolution carbon and sulfur isotope records of the evolving Paleozoic marine sulfur reservoir. Palaeogeogr. Palaeoclimatol. Palaeoecol. 256, 156–173.
Gill, B.C., Lyons, T.W., Jenkyns, H.C., 2011. A global perturbation to the sulfur cycle during the Toarcian Oceanic Anoxic Event. Earth Planet. Sci. Lett. 312, 484–496.
Gill, B.C., Dahl, T.W., Hammarlund, E.U., LeRoy, M.A., Gordon, G.W., Canfield, D.E., Anbar, A.D., Lyons, T.W., 2021. Redox dynamics of later Cambrian oceans. Palaeogeogr. Palaeoclimatol. Palaeoecol. 581, 110623.
Gomes, M.L., Hurtgen, M.T., 2015. Sulfur isotope fractionation in modern euxinic systems: implications for paleoenvironmental reconstructions of paired sulfate–sulfide isotope records. Geochim. Cosmochim. Acta 157, 39–55.
Hardisty, D.S., Lyons, T.W., Riedinger, N., Isson, T.T., Owens, J.D., Aller, R.C., Rye, D.M., Planavsky, N.J., Reinhard, C.T., Gill, B.C., 2018. An evaluation of sedimentary molybdenum and iron as proxies for pore fluid paleoredox conditions. Am. J. Sci. 318, 527–556.
Harrison, J., Mayr, U., McNeil, D., Sweet, A., Eberle, J., McIntyre, D., Harington, C., Chalmers, J., Dam, G., Nøhr-Hansen, H., 1999. Correlation of Cenozoic sequences of the Canadian Arctic region and Greenland; implications for the tectonic history of northern North America. Bull. Can. Petrol. Geol. 47, 223–254.
Hints, O., Antonovitš, L., Bauert, G., Nestor, V., Nõlvak, J., Tammekänd, M., 2018. CHITDB: a database for documenting and analysing diversification of Ordovician–Silurian chitinozoans in the Baltic region. Lethaia 51, 218–227.
Jaeger, H., 1959. Grapholithen und Stratigraphie des jüngsten Thüringer Silurs. Akademie-Verlag.
Jeppsson, L., 1998. Silurian oceanic events: summary of general characteristics. N. Y. State Mus. Bull. 491, 239–257.
Jeppsson, L., Calner, M., 2002. The Silurian Mulde Event and a scenario for secundo–secundo events. Earth Environ. Sci. Trans. R. Soc. Edinb. 93, 135–154.
Johnson, M.E., 2010. Tracking Silurian eustasy: Alignment of empirical evidence or pursuit of deductive reasoning?. In: Early Palaeozoic Sea Level and Climate, 296, pp. 276–284.
Kaljo, D., Märss, T., 1991. Pattern of some Silurian bioevents. Hist. Biol. 5, 145–152.

Kaljo, D., Boucot, A.J., Corfield, R.M., Herisse, A.L., Koren, T.N., Kriz, J., Männik, P., Märss, T., Nestor, V., Shaver, R.H., 1996. Silurian bio-events. In: Global Events and Event Stratigraphy in the Phanerozoic: Results of the International Interdisciplinary Cooperation in the IGCP-Project 216 "Global Biological Events in Earth History", pp. 173–224.
Kaljo, D., Kiipli, T., Martma, T., 1997. Carbon isotope event markers through the Wenlock–Pridoli sequence at Ohesaare (Estonia) and Priekule (Latvia). Palaeogeogr. Palaeoclimatol. Palaeoecol. 132, 211–223.
Kiipli, T., Kiipli, E., Kaljo, D., 2010. Silurian Sea level variations estimated using SiO2/Al2O3 and K2O/Al2O3 ratios in the Priekule drill core section, Latvia. Boll. Soc. Paleontol. Ital. 49, 55–63.
Koren, T., 1991. The lundgreni extinction event in central Asia and its bearing on graptolite biochronology within the Homerian. In: Presented at the Proceedings of the Estonian Academy of Sciences, Geology. Estonian Academy Publishers, pp. 74–78.
Kozik, N.P., Gill, B.C., Owens, J.D., Lyons, T.W., Young, S.A., 2022a. Geochemical records reveal protracted and differential marine redox change associated with late ordovician climate and mass extinctions. AGU Adv. 3, e2021AV000563.
Kozik, N.P., Young, S.A., Newby, S.M., Liu, M., Chen, D., Hammarlund, E.U., Bond, D.P. G., Them, T.R., Owens, J.D., 2022b. Rapid marine oxygen variability: driver of the late Ordovician mass extinction. Sci. Adv. 8, eabn8345.
Kozik, N.P., Young, S.A., Lindskog, A., Ahlberg, P., Owens, J.D., 2023. Protracted oxygenation across the Cambrian–Ordovician transition: a key initiator of the Great Ordovician Biodiversification Event? Geobiology 21, 323–340.
Krause, A.J., Mills, B.J.W., Zhang, S., Planavsky, N.J., Lenton, T.M., Poulton, S.W., 2018. Stepwise oxygenation of the Paleozoic atmosphere. Nat. Commun. 9, 4081.
Lenz, A.C., Noble, P.J., Masiak, M., Poulson, S.R., Kozłowska, A., 2006. The lundgreni Extinction Event: integration of paleontological and geochemical data from Arctic Canada. Gff 128, 153–158.
Lyons, T.W., Gill, B.C., 2010. Ancient sulfur cycling and oxygenation of the early biosphere. Elements 6, 93–99.
Lyons, T.W., Severmann, S., 2006. A critical look at iron paleoredox proxies: new insights from modern euxinic marine basins. Geochim. Cosmochim. Acta 70, 5698–5722.
Lyons, T.W., Anbar, A.D., Severmann, S., Scott, C., Gill, B.C., 2009. Tracking Euxinia in the Ancient Ocean: a multiproxy perspective and proterozoic case study. Annu. Rev. Earth Planet. Sci. 37, 507–534.
Manda, Š., Štorch, P., Frýda, J., Slavík, L., Tasáryová, Z., 2019. The mid-Homerian (Silurian) biotic crisis in offshore settings of the Prague Synform, Czech Republic: integration of the graptolite fossil record with conodonts, shelly fauna and carbon isotope data. Palaeogeogr. Palaeoclimatol. Palaeoecol. 528, 14–34.
März, C., Poulton, S.W., Beckmann, B., Küster, K., Wagner, T., Kasten, S., 2008. Redox sensitivity of P cycling during marine black shale formation: dynamics of sulfidic and anoxic, non-sulfidic bottom waters. Geochim. Cosmochim. Acta 72, 3703–3717.
McAdams, N.E., Cramer, B.D., Bancroft, A.M., Melchin, M.J., Devera, J.A., Day, J.E., 2019. Integrated δ13Ccarb, conodont, and graptolite biochemostratigraphy of the Silurian from the Illinois Basin and stratigraphic revision of the Bainbridge Group. Bulletin 131, 335–352.
Melchin, M.J., Mitchell, C.E., Holmden, C., Štorch, P., 2013. Environmental changes in the late Ordovician–early Silurian: review and new insights from black shales and nitrogen isotopes. Bulletin 125, 1635–1670.
Melchin, M.J., Sadler, P.M., Cramer, B.D., 2020. Chapter 21 - the Silurian Period. In: Gradstein, F.M., Ogg, J.G., Schmitz, M.D., Ogg, G.M. (Eds.), Geologic Time Scale 2020. Elsevier, pp. 695–732.
Miller, C.A., Peucker-Ehrenbrink, B., Walker, B.D., Marcantonio, F., 2011. Re-assessing the surface cycling of molybdenum and rhenium. Geochim. Cosmochim. Acta 75, 7146–7179.
Morford, J.L., Emerson, S., 1999. The geochemistry of redox sensitive trace metals in sediments. Geochim. Cosmochim. Acta 63, 1735–1750.
Munnecke, A., Calner, M., Harper, D.A., Servais, T., 2010. Ordovician and Silurian Sea–water chemistry, sea level, and climate: a synopsis. Palaeogeogr. Palaeoclimatol. Palaeoecol. 296, 389–413.
Noble, P.J., Zimmerman, M.K., Holmden, C., Lenz, A.C., 2005. Early Silurian (Wenlockian) δ13C profiles from the Cape Phillips Formation, Arctic Canada and their relation to biotic events. Can. J. Earth Sci. 42, 1419–1430.
Noble, P.J., Lenz, A.C., Holmden, C., Masiak, M., Zimmerman, M.K., Poulson, S.R., Kozłowska, A., 2012. Isotope Geochemistry and Plankton Response to the Ireviken (Earliest Wenlock) and Cyrtograptus lundgreni Extinction events, Cape Phillips Formation, Arctic Canada. Earth Life 631–652.
Owens, J.D., Reinhard, C.T., Rohrssen, M., Love, G.D., Lyons, T.W., 2016. Empirical links between trace metal cycling and marine microbial ecology during a large perturbation to Earth's carbon cycle. Earth Planet. Sci. Lett. 449, 407–417.
Owens, J.D., Lyons, T.W., Hardisty, D.S., Lowery, C.M., Lu, Z., Lee, B., Jenkyns, H.C., 2017. Patterns of local and global redox variability during the Cenomanian–Turonian Boundary Event (Oceanic Anoxic Event 2) recorded in carbonates and shales from central Italy. Sedimentology 64, 168–185.
Pasquier, V., Sansjofre, P., Rabineau, M., Revillon, S., Houghton, J., Fike, D.A., 2017. Pyrite sulfur isotopes reveal glacial– interglacial environmental changes. Proc. Natl. Acad. Sci. 114, 5941–5945.
Porębska, E., Kozłowska-Dawidziuk, A., Masiak, M., 2004. The lundgreni event in the Silurian of the east European Platform, Poland. Palaeogeogr. Palaeoclimatol. Palaeoecol. 213, 271–294.
Poulton, S.W., 2021. The iron speciation paleoredox proxy. In: Elements in Geochemical Tracers in Earth System Science. Cambridge University Press, Cambridge.
Poulton, S.W., Canfield, D.E., 2005. Development of a sequential extraction procedure for iron: implications for iron partitioning in continentally derived particulates. Chem. Geol. 214, 209–221.
Poulton, S.W., Canfield, D.E., 2011. Ferruginous conditions: a dominant feature of the ocean through Earth's history. Elements 7, 107–112.
Poulton, S.W., Raiswell, R., 2002. The low-temperature geochemical cycle of iron: from continental fluxes to marine sediment deposition. Am. J. Sci. 302, 774–805.
Poulton, S.W., Krom, M.D., Raiswell, R., 2004. A revised scheme for the reactivity of iron (oxyhydr) oxide minerals towards dissolved sulfide. Geochim. Cosmochim. Acta 68, 3703–3715.
Raiswell, R., Canfield, D.E., 1998. Sources of iron for pyrite formation in marine sediments. Am. J. Sci. 298, 219–245.
Raiswell, R., Canfield, D.E., 2012. The iron biogeochemical cycle past and present. Geochem. Perspect. 1, 1–2.
Raiswell, R., Hardisty, D.S., Lyons, T.W., Canfield, D.E., Owens, J.D., Planavsky, N.J., Poulton, S.W., Reinhard, C.T., 2018. The iron paleoredox proxies: a guide to the pitfalls, problems and proper practice. Am. J. Sci. 318, 491–526.
Ray, D.C., Jarochowska, E., Röstel, P., Worton, G., Munnecke, A., Wheeley, J.R., Boomer, I., 2019. High-resolution correlation of the Homerian carbon isotope excursion (Silurian) across the interior of the Midland Platform (Avalonia), UK. Geol. Mag. 157, 603–620.
Reinhard, C.T., Planavsky, N.J., Robbins, L.J., Partin, C.A., Gill, B.C., Lalonde, S.V., Bekker, A., Konhauser, K.O., Lyons, T.W., 2013. Proterozoic Ocean redox and biogeochemical stasis. Proc. Natl. Acad. Sci. 110, 5357–5362.
Rue, E.L., Smith, G.J., Cutter, G.A., Bruland, K.W., 1997. The response of trace element redox couples to suboxic conditions in the water column. Deep-Sea Res. I Oceanogr. Res. Pap. 44, 113–134.
Saltzman, M.R., 2001. Silurian δ13C stratigraphy: a view from North America. Geology 29, 671–674.
Scotese, C., 2014. Atlas of Silurian and Middle-Late Ordovician Paleogeographic Maps (Mollweide Projection), Maps 73–80, Volumes 5, the Early Paleozoic, PALEOMAP Atlas for ArcGIS. PALEOMAP Project.
Scott, C., Lyons, T.W., 2012. Contrasting molybdenum cycling and isotopic properties in euxinic versus non-euxinic sediments and sedimentary rocks: refining the paleoproxies. Chem. Geol. 324, 19–27.
Sproson, A.D., Pogge von Strandmann, P.A.E., Selby, D., Jarochowska, E., Frýda, J., Hladil, J., Loydell, D.K., Slavík, L., Calner, M., Maier, G., Munnecke, A., Lenton, T. M., 2022. Osmium and lithium isotope evidence for weathering feedbacks linked to orbitally paced organic carbon burial and Silurian glaciations. Earth Planet. Sci. Lett. 577, 117260.
Stockey, R.G., Cole, D.B., Planavsky, N.J., Loydell, D.K., Frýda, J., Sperling, E.A., 2020. Persistent global marine euxinia in the early Silurian. Nat. Commun. 11, 1804.
Štorch, P., 1995. Biotic crises and post-crisis recoveries recorded by Silurian planktonic graptolite faunas of the Barrandian area (Czech Republic). Geolines 3, 59–70.
Taylor, S.R., McLennan, S.M., 1995. The geochemical evolution of the continental crust. Rev. Geophys. 33, 241–265.
Trettin, H., 1989. The Arctic Islands. In: Bally, A.W., Palmer, A.R. (Eds.), The Geology of North America. Decade of North American Geology, pp. 349–370.
Tribovillard, N., Algeo, T.J., Lyons, T., Riboulleau, A., 2006. Trace metals as paleoredox and paleoproductivity proxies: an update. Chem. Geol. 232, 12–32.
Trotter, J.A., Williams, I.S., Barnes, C.R., Männik, P., Simpson, A., 2016. New conodont δ18O records of Silurian climate change: implications for environmental and biological events. Palaeogeogr. Palaeoclimatol. Palaeoecol. 443, 34–48.
Turgeon, S., Brumsack, H.-J., 2006. Anoxic vs dysoxic events reflected in sediment geochemistry during the Cenomanian–Turonian Boundary Event (Cretaceous) in the Umbria–Marche Basin of central Italy. Chem. Geol. 234, 321–339.
Wang, Y., Wignall, P.B., Xiong, Y., Loydell, D.K., Peakall, J., Baas, J.H., Mills, B.J., Poulton, S.W., 2024. Marine redox dynamics and biotic response to the mid-Silurian Ireviken Extinction Event in a mid-shelf setting. J. Geol. Soc. Lond. 181, jgs2023-155.
Young, S.A., Kleinberg, A., Owens, J.D., 2019. Geochemical evidence for expansion of marine euxinia during an early Silurian (Llandovery–Wenlock boundary) mass extinction. Earth Planet. Sci. Lett. 513, 187–196.
Young, S.A., Benayoun, E., Kozik, N.P., Hints, O., Martma, T., Bergström, S.M., Owens, J. D., 2020. Marine redox variability from Baltica during extinction events in the latest Ordovician–early Silurian. Palaeogeogr. Palaeoclimatol. Palaeoecol. 554, 109792.
Zou, C., Qiu, Z., Poulton, S.W., Dong, D., Wang, H., Chen, D., Lu, B., Shi, Z., Tao, H., 2018. Ocean euxinia and climate change "double whammy" drove the late Ordovician mass extinction. Geology 46, 535–538.